Journal Pre-proof

Degradation and mineralization of erythromycin by heterogeneous photocatalysis using SnO 2-doped TiO$_2$ structured catalysts: activity and stability

L.L. Albornoz, S.W. da Silva, J.P. Bortolozzi, E.D. Banús, P. Brussino, M.A. Ulla, A.M. Bernardes

CREDIT AUTHOR STATEMENT

Albornoz L. L.: Conceptualization, Methodology, Validation, Investigation, Data Curation, Writing – Original Draft and Writing – Review & Editing

da Silva S. W.: Conceptualization, Methodology, Investigation, Validation, Formal analysis, Data Curation, Writing – Original Draft and Writing – Review & Editing

Bortolozzi J. P.: Investigation, Validation and Writing – Original Draft

Banús E. D.: Supervision, Investigation, Methodology and Writing – Review & Editing

Brussino, P.: Investigation, Validation and Writing – Review & Editing

Ulla M. A: Resources, Funding acquisition and Writing – Review & Editing and Supervision.

Bernardes A. M.: Resources, Project administration, Funding acquisition, Supervision, Writing – Original Draft and Writing – Review & Editing
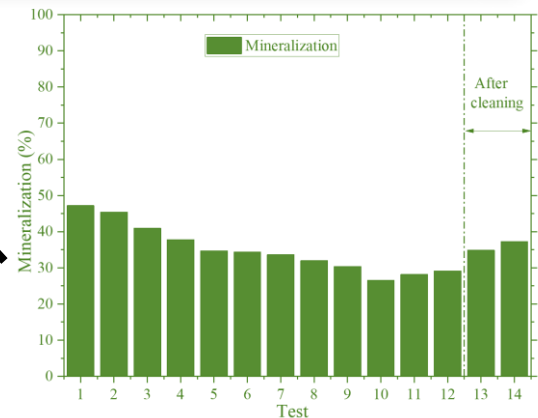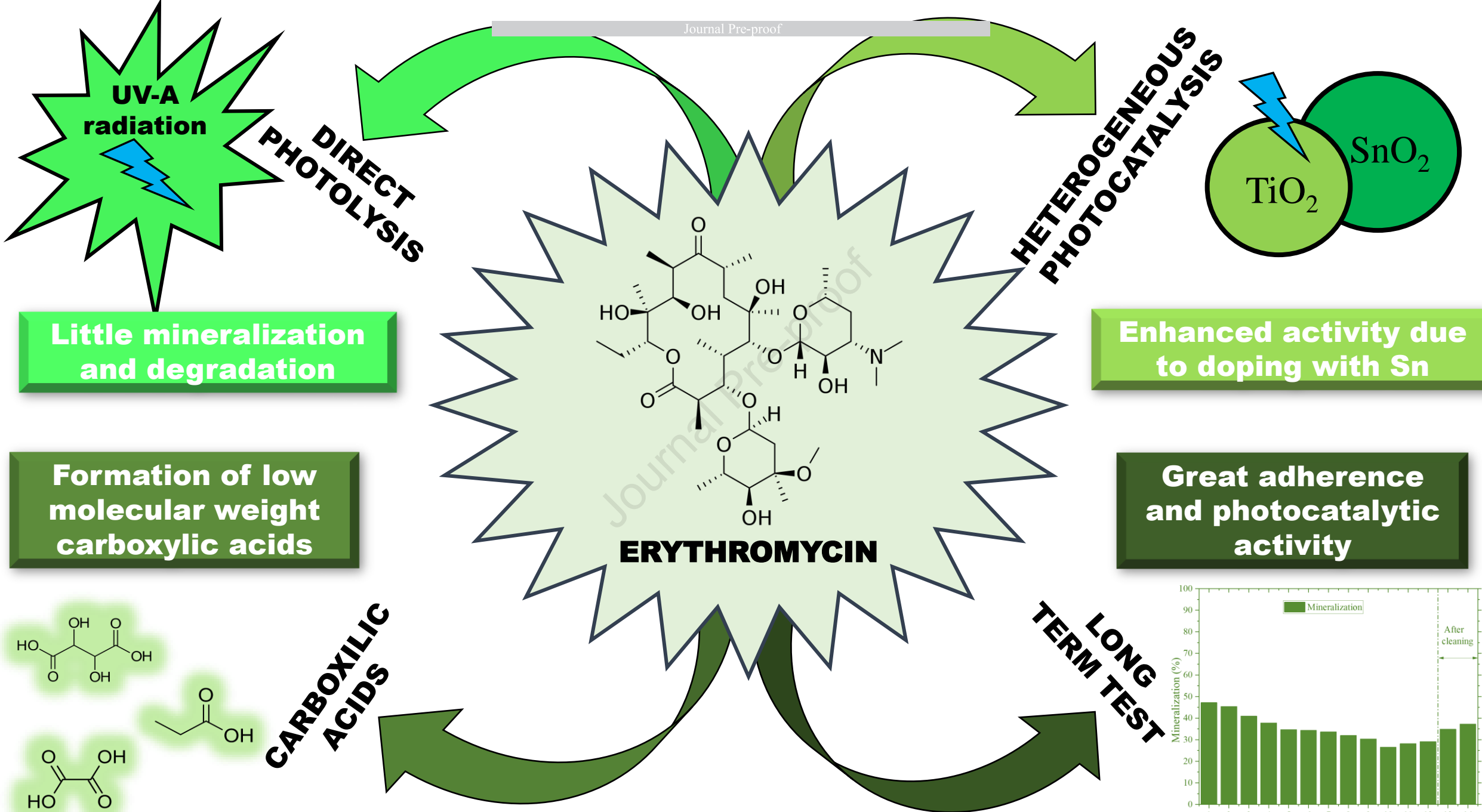
UV-A radiation

DIRECT PHOTOLYSIS

HETEROGENEOUS PHOTOCATALYSIS

TiO_2

SnO_2

Little mineralization and degradation

Enhanced activity due to doping with Sn

Formation of low molecular weight carboxylic acids

Great adherence and photocatalytic activity

ERYTHROMYCIN

CARBOXILIC ACIDS

LONG TERM TEST

Degradation and mineralization of erythromycin by heterogeneous photocatalysis using

SnO$_2$-doped TiO$_2$ structured catalysts: activity and stability

Albornoz L. L. [a,b], da Silva S. W.[b*], Bortolozzi J. P.[c], Banús E. D.[c], Brussino, P.[c], Ulla M. A.[c],

Bernardes A. M.[a]

[a] Universidade Federal do Rio Grande do Sul (UFRGS), Programa de Pós-Graduação em Engenharia de Minas, Metalúrgica e de Materiais (PPGEM), Av. Bento Gonçalves, 9500, Porto Alegre, RS, Brazil.

[b] UFRGS, Instituto de Pesquisas Hidráulicas (IPH), Programa de Pós-Graduação em Recursos Hídricos e Saneamento Ambiental, Av. Bento Gonçalves, 9500, Porto Alegre, RS, Brazil.

[c] Instituto de Investigaciones en Catálisis y Petroquímica – INCAPE (UNL – CONICET), Santiago del Estero 2829, 3000 Santa Fe, Argentina.

*Corresponding author: salatiel.silva@ufrgs.br

ABSTRACT

Heterogeneous photocatalysis was used for the degradation and mineralization of erythromycin (ERY), with a consequent production of carboxylic acids. For that, a series of TiO$_2$ and Ti$_{1-x}$Sn$_x$O$_2$ structured catalysts, namely M1 to M5, was prepared using the washcoating method, with the catalytic coatings being deposited onto stainless steel meshes. Besides, the catalytic activity of the prepared systems was compared to that of the commercial mesh (CM). The results showed that the prepared TiO$_2$ structured catalyst (M1) presented better ERY oxidation than the CM one, what was associated to the higher catalyst load and to the anatase/rutile ratio. Considering the Sn-doped structured catalysts, for M2, M4 and M5 catalysts, lower ERY mineralization and high formation of

carboxylic acids were found, when compared to the M3 catalyst. The improved M3 activity was attributed to the formation of a staggered gap (type II heterojunction), providing better charge separation. In this situation, a high generation of hydroxyl radicals is obtained, resulting on a higher ERY mineralization. By the obtained results it is possible to determine that the addition order and the type of Sn compound added in the washcoating process, affects the catalytic activity due to the formation of a solid solution and to the type of produced heterostructures. The M3 catalyst also showed high stability in long-term tests up to 44 h of reaction. The results provide insights into the development of an inexpensive structured catalyst production method and its influence in the stability of the photocatalyst, as well as in its applicability on water/wastewater treatment.

KEYWORDS: $Ti_{1-x}Sn_xO_2$; Washcoating; Photocatalysis; Erythromycin; Short carboxylic acids.

1   INTRODUCTION

Contaminants of emerging concern (CEC), whose effects on the ecosystem and on human health are unknown or not well understood, have been found in different environments because they are not removed by conventional techniques (Barrios-Estrada et al., 2018; Gogoi et al., 2018; Rodriguez-Narvaez et al., 2017). One example of the CEC is erythromycin (ERY), which is used by people who are allergic to penicillin and it can remain in nature for up to one year, maintaining its antibiotic activity (Patel et al., 2019). After its administration, the degradation within the human body occurs via the biliary and renal tract, the first being the major route of excretion. However, more than 60 % of ERY, as well as other macrolides, is excreted unchanged (Babić et al., 2017).
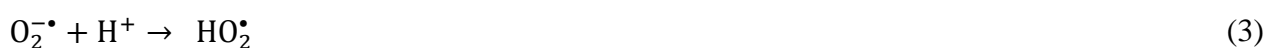
The United States Environmental Protection Agency in 2009 included ERY on its Contaminant Candidate List 3 (CCL 3), while the European Union through its Decision 2015/495/EU, included ERY as a high-risk priority substance (European Comission, 2017). According to Li et al. (2014), in a ranking developed in China, ERY was identified as a

53 pharmaceutical with a high priority for environmental control due to its recurrent detection in

54 sewage   effluents   or   in   water   supplies

55 (Lin and Tsai, 2009). ERY was detected in water sources (Westerhoff et al., 2005), affluents of

56 wastewater treatment plants (WWTP) (Hapeshi et al., 2015), effluents of WWTP

57 (Rühmland et al., 2015); natural waters (Pico et al., 2019) and underground waters (Lin et al.,

58 2015). Like other CEC, ERY is not well removed by conventional treatment processes; therefore, it

59 must be removed through more complex technologies like advanced oxidative processes (AOP)

60 (Stackelberg et al, 2007; Yang et al., 2017). Heterogeneous photocatalysis (HP) was developed with

61 this objective. The degradation by HP occurs due to the formation of species with high oxidation

62 potential (HO$^\bullet$, O$_2^{-\bullet}$) that perform the oxidation to simpler compounds, leading to mineralization

63 (Andreozzi et al., 1999; Kanakaraju et al., 2018).

64   During the HP process, the irradiation of the catalyst surface leads to the adsorption of

65 energy, transferring one electron (e_{vb}^-) of the valence band (VB) to the conduction band (CB) (e_{cb}^-),

66 generating a hole (h_{vb}^+) in the VB (Eq. (1)) (Vignesh et al., 2014; Voigt and Jaeger , 2017).

$$TiO_2 \xrightarrow{h\nu} TiO_2 \ (h_{vb}^+ + e_{cb}^-) \tag{1}$$

67   After the formation of the pair e_{cb}^-/h_{vb}^+, two processes may occur: (i) an internal

68 recombination, releasing thermal energy and/or luminance, bringing the catalyst back to its original

69 condition; (ii) with the system excited, reactions 2 to 5 will occur in CB (Vignesh et al., 2014;

70 Voigt and Jaeger , 2017), generating species with high oxidation potential.

$$e_{cb}^- + O_2 \rightarrow \ O_2^{-\bullet} \tag{2}$$

$$O_2^{-\bullet} + H^+ \rightarrow \ HO_2^\bullet \tag{3}$$

$$HO_2^\bullet + HO_2^\bullet \rightarrow H_2O_2 + O_2 \tag{4}$$

$$e_{cb}^- + H_2O_2 \rightarrow OH^- + HO^\bullet \tag{5}$$

71   Besides, in the VB direct oxidation can occur by transferring e$^-$ from the molecules that are

72 adsorbed on the catalyst surface to the h_{vb}^+. Due to the low concentrations of organic matter in

73 solution, the main oxidation reactions that occur on the catalyst surface are from adsorbed water or

74 hydroxide anion molecules (Eq. 6 and 7). Nevertheless, the oxidation reaction of organic matter

75 (M_{ads}), also occurs on the catalyst surface (Eq. 8), providing another route for $HO^{\bullet}$ generation

76 (Vignesh et al., 2014; Voigt and Jaeger, 2017).

$$h_{vb}^{+} + H_2O_{ads} \rightarrow HO_{ads}^{\bullet} + H^{+} \tag{6}$$

$$h_{vb}^{+} + OH_{ads}^{-} \rightarrow HO_{ads}^{\bullet} \tag{7}$$

$$h_{vb}^{+} + M_{ads} \rightarrow HO_{ads}^{\bullet} + M_{ads}^{\bullet} \tag{8}$$

77 TiO$_2$ Degussa P 25 is a semiconductor widely used in HP processes because of its high

78 stability, non-toxicity and high photocatalytic efficiency compared to other semiconductors

79 (Babić et al., 2017), due to its composition of 80 % anatase and 20 % rutile (Rui et al., 2014).

80 However, TiO$_2$ presents a high e_{cb}^{-}/h_{vb}^{+} recombination rate, decreasing the oxidation efficiency and

81 causing energy loss (Pesci et al., 2013; Shen et al., 2018).

82 Several materials are used as TiO$_2$ dopants aiming for the reduction of the bandgap and the

83 increase of the lifetime of the charges, leading to higher oxidation efficiencies. However,

84 conventional dopants such as ruthenium (Ru), tungsten (W), niobium (Nb) and cerium (Ce) are

85 classified as critical materials by the European Union (Choi et al., 1994; European Comission,

86 2017; Solís-Casados et al., 2017; Zhou et al., 2016).

87 Therefore, it is interesting to develop materials with dopants that are not considered critical

88 elements (European Comission, 2017). Tin (Sn) can be used for doping TiO$_2$ to decrease the

89 recombination of the e_{cb}^{-}/h_{vb}^{+} pair, allowing the degradation of complex contaminants

90 (Kusior et al., 2019; Pesci et al., 2013). Doping occurs by replacing a Ti atom with a Sn atom or by

91 inserting a Sn atom into an empty interstitial space in the TiO$_2$ unit cell. Both processes are favored

92 due to the similarity of the atomic radius sizes, electronic valence (+4) and crystalline structures,

93 allowing the formation of a Ti$_{1-x}$Sn$_x$O$_2$ solid solution (Kusior et al., 2019) with the generation of a

94 type II heterojunction, where an effective charge separation on the VB and CB can be generated

95 (Del Angel et al., 2018; Kusior et al., 2019).

96   Different studies performed the doping of SnO_2 in the TiO_2 unit cell using different coating

97   preparation methodologies (hydrothermal, microwave-assisted and sol gel synthesis) and AOP

98   processes (heterogeneous photocatalysis and photoelectrochemical) in the degradation of different

99   CEC (methylene blue, diclofenac, methyl orange, zopiclone and acid orange 7). These studies

100   showed that there is an effective increase in the photocatalytic activity of TiO_2 when doped with

101   SnO_2

102   (Kusior et al., 2019, Mugunthan et al., 2019; Sangchay, 2016; Vinodgopal and Kamat 1995;

103   Yu et al., 2013).

104   However, Sn-doped TiO_2 structured catalysts prepared by washcoating of stainless steel

105   meshes, and their subsequent use in the mineralization and degradation of ERY through HP, have

106   not been reported in the literature to our knowledge. Therefore, this work presents different

107   procedures of doping TiO_2 with SnO_2 through the washcoating method applied to AISI 304 meshes,

108   which ended up not only in different Sn/Ti distributions on the photocatalytic coating but also in

109   different Ti-Sn interactions. The main goal is focused in the evaluation of the photocatalytic activity

110   of these structured catalysts in the degradation of ERY with UV-A radiation. The quality and

111   efficiency of the coatings were assessed through long-term tests and by the analysis of the formation

112   of carboxylic acids. Furthermore, a reaction mechanism was proposed.

113

114   **2   EXPERIMENTAL**

115   **2.1   Materials, synthesis and characterization**

116   A series of titanium and titanium/tin oxides structured catalysts with a PVA/TiO_2 mass ratio

117   of 0.37 were synthesized through the washcoating method applied to structured substrates (AISI

118   304 meshes) (Trindade et al. 2018). All solvents and reagents used were of analytical grade.

119   AEROXIDE® TiO_2 P 25 (Evonik), ZrO_2 (Zr10/15) and SnO_2 (SN15) from Nyacol®, tin (II) oxalate

120   and polyvinyl alcohol from Sigma-Aldrich were used to prepare catalysts by the washcoating

121   method. AISI 304 stainless steel meshes (opening 0.546 mm and 0.30 mm wire diameter) were used

122   as substrates for the catalyst coatings. In addition, a commercial mesh photocatalyst designated as

123   CM with a $Ti_{0.7}Ru_{0.3}O_2$–Ti composition (with a geometrical surface area of 475.2 cm^2) was used as

124   a comparison to the prepared photocatalysts.

125   The substrates were cut into a rectangular shape with 6 cm in width $\times$ 16 cm in length with a

126   geometrical surface area of 212.89 cm^2. Due to the setup that was adopted for the photocatalytic

127   tests, the substrates were shaped into a hemi cylindrical form with $\varnothing = 10$ cm. The AISI 304 mesh

128   pieces (structured substrates) were cleaned and pretreated through a calcination to generate an

129   oxidic layer which allows the posterior coatings anchoring, according to Bortolozzi et al. (2010).

130   Subsequently, the washcoating method was used to immobilize the photocatalytic coatings

131   onto the metallic mesh pieces, following four basic steps described elsewhere (Trindade et al.,

132   2018): (i) dip, (ii) blowing, (iii) drying and (iv) calcination. The basic washcoating suspension

133   composition was: 121.2 g H_2O, 3.6 g PVA, 40.8 g ZrO_2 and 9.6 g TiO_2. Five different structured

134   catalysts were obtained: M1, M2, M3, M4 and M5. M1 was prepared with the basic suspension

135   composition (free of Sn). For the other structured catalysts, the preparation consisted in the

136   incorporation of Sn to the catalytic coating via different methods and Sn sources: 1) M2: after

137   obtaining the TiO_2 coating (M1), Sn was impregnated on M1 via its immersion in an aqueous

138   solution of Sn oxalate (0.5 g L^{-1}); 2) M3: Sn oxalate was added to the basic washcoating suspension

139   along with the others components; 3) M4: powder microparticles of SnO_2 were incorporated to the

140   basic washcoating suspension; 4) M5: the same methodology as M3 and M4 was applied, but using

141   a suspension of SnO_2 nanoparticles (Nyacol SN15). A detailed experimental procedure is shown in

142   the supplementary material (Fig. S1).

143   Surface images were obtained after each calcination step for all structured catalysts during

144   the coating process, as previously described and shown in Fig. S1. Optical microscopy was

145   performed with a Leica S8 APO microscope equipped with a Leica LC3 digital camera and LAS EZ

146   software. The surface images were analyzed to determine the quality of the coatings and taken into

147   account to define the number of immersions and calcination cycles for each catalyst.

148   The surface features of the prepared systems were characterized by scanning electron

149 microscopy (SEM) equipped with an energy dispersive X-ray (EDS) detector (Phenom ProX

150 Desktop SEM equipment, ThermoFisher). The elemental mappings were performed on a Phenom

151 ProX Desktop SEM software and operating at 15 kV. Several sectors were analyzed, and all the

152 components were taken into account to estimate the Sn/Ti ratios and to obtain a better picture of the

153 elements distribution.

154   The crystalline phases were identified using X-ray diffraction (XRD), the equipment being a

155 Shimadzu XD-D1 with Cu Kα radiation. Every XRD experiment was ran at a scan rate of $2°$ min^{-1},

156 from $2\theta = 20°$ to $80°$.

157   X-ray Photoelectron Spectroscopy (XPS) was used to analyze the surface Sn species. A

158 SPECS spectrometer equipment with a hemispherical PHOIBOS 150 analyzer operated in the FAT

159 mode (30 eV, 200W, Mg Kα X-ray source power) was used. The samples were evacuated in

160 vacuum at 10^{-3} mbar at 200 °C for 10 min. Then, they were evacuated for 120 min in ultra-high

161 vacuum. The peak fitting was performed with the CASAXPS software using C 1s at 284.6 eV as

162 reference.

163

164 **2.2 Photocatalytic evaluation**

165   The performance of the structured catalysts was evaluated in the heterogeneous

166 photocatalysis (HP) for the oxidation of ERY. The ERY solution had a concentration of 50 mg L^{-1}

167 and was prepared by dissolving ERY estolate in deionized water. The tests were carried out adding

168 1 L of ERY solution - pH 5.4 - in the non-irradiated reservoir that fed the 0.3 L home-made photo-

169 reactor with a flowrate of 1.2 L min^{-1} (Fig. 1). A 9 W UV-A lamp (Dulux S BL UVA 9 W/78) was

170 placed in the center of the reactor, which was surrounded by two structured catalysts in a concentric

171 arrangement. The distances from the lamp to the catalyst as well as from the catalysts to the reactor

172 walls were set at 2 cm.

173   To get better insights about the ERY removal mechanism, adsorption (ADS) and direct

174   photolysis (DP) tests were also conducted. For ADS tests the UV-A lamp was turned off, while the

175   structured catalysts were removed for the DP assays. In all cases (HP, ADS and DP), duplicate 240-

176   minute tests were performed and, if necessary, additional tests were carried out.

177   The stability of the structured catalyst that presented the best results in ERY mineralization

178   was also evaluated. For that, the structured catalyst was subjected to HP experiments fourteen times

179   in the same conditions and reactor, only replacing the ERY solution after each test. After the 14

180   experiments, the structured catalyst was evaluated to determine the catalyst stability.

181   **Figure 1.**

182

183   **2.3   Analytical**

184   Tests of 240 minutes were performed, and aliquots were collected at 0, 5, 15, 30, 60, 120,

185   180 and 240 minutes for measurements of pH, total organic carbon (TOC) and high-performance

186   liquid chromatography (HPLC) analysis at room temperature. pH measurements were performed

187   with a digital instrument (KASVI K39-0014PA) calibrated with standards of 4, 7 and 10. TOC

188   analysis was made on a TOC-L CPH Shimadzu apparatus with the Non-Purgeable Organic Carbon

189   (NPOC) method, according to the instructions of the TOC Shimadzu manual.

190   The ERY decay and the generation of carboxylic acids were detected in a HPLC Shimadzu

191   LC20A apparatus with a diode array detector (DAD) SPD-20AV and an autosampler SIL-20A. For

192   ERY detection, the HPLC was fitted with a Shim-pack XR-ODS C18 (3.0 mm ID $\times$ 50 mm,

193   Shimadzu) column. As mobile phase-A a 0.025 M phosphate buffer (pH 2.5) was used and as

194   mobile phase-B acetonitrile was used. The analyses were performed in isocratic mode, with 40 % of

195   the mobile phase-A and 60 % of the mobile phase-B at a flow rate of 1.0 mL min^{-1}. 20 µL of the

196   sample were injected and the DAD was set in $\lambda = 210$ nm. In these conditions, the ERY retention

197   time was 4.8 min.

198   The generated carboxylic acids were detected by ion-exclusion HPLC using a Rezex Roa-

199   Organic acid H^+ (8 %, 100×4.6 mm) column and the DAD was set at $\lambda = 210$ nm. These

200   measurements were performed by injecting 20 µL of the samples into the HPLC and using a

201   0.05 M H_2SO_4 solution as mobile phase, at a flow rate of 0.1 mL min^{-1}. At these conditions, ion

202   exclusion chromatography exhibited peaks related to oxalic, tartaric, formic, acetic, propionic and

203   isovaleric acids, at retention times of 6.16, 7.78, 11.65, 12.65, 14.75 and 20.82 min, respectively.

204

205   **3   RESULTS AND DISCUSSION**

206   **3.1 Adsorption and photocatalytic tests**

207   The ADS test is an important step in catalytic processes, considering that oxidation and

208   reduction reactions will happen just for molecules that are in direct contact with the catalyst surface,

209   where the radicals are produced (Gaya and Abdullah, 2008; Humayun et al., 2018). Therefore, the

210   ADS tests in Fig. 2a indicate that the different adsorption behavior of the catalysts probably will

211   induce different ERY removal rates by photocatalysis. It was observed that the commercial mesh

212   catalyst (CM) presented the worst ADS results, when compared to all catalysts prepared by the

213   washcoating method. This infers that the method used in the catalysts preparation may have an

214   effect on the surface area, pore geometrical structure and catalyst loading (Thomas and Thomas,

215   2015), influencing the ADS process.

216   Besides, the M3 catalyst exhibited better ADS properties than the other catalysts prepared

217   by washcoating, indicating that the order of the addition or the tin source used in the washcoating

218   procedure have an influence on the ADS results. For the M3 catalyst, the addition of tin oxalate into

219   the washcoating suspension probably led to the formation of a high-quality solid solution which

220   results in a better ADS process. Furthermore, after 60 min of ADS tests the ERY concentration

221   presented   little   variation,   which   may   indicate   a   saturation   of   the   catalyst   surface

222   (Konstantinou and Albani, 2004; Tong et al., 2012).

223   A study conducted by Karaolia et al. (2018) showed that the ERY adsorption onto TiO_2

224   Degussa P25 is low and only 7 % of ERY degradation occurs on the surface of the immobilized

225   catalyst. The authors attributed the low ERY adsorption to the low electrostatic attraction of the

226   TiO_2 Degussa P25 surface with ERY, because ERY does not have $\pi - \pi$ bonds in its structure, a

227   characteristic that would favor polarization and electrostatic attraction between the surface of TiO_2

228   Degussa P25 and ERY. The low specific surface area and porosity of TiO_2 are characteristics that

229   may also explain the low ADS of ERY (Ayoub et al., 2019).

230   On the other hand, Sn-doped TiO_2 shows better adsorption due to the fact that the addition

231   of Sn in the crystalline network of titania causes an increase in the photocatalyst surface area and a

232   height reduction of the grain boundary electron barrier, allowing a greater electron transfer from

233   ERY into the photocatalyst (Krishnan et al., 2017). Therefore, the conductivity of this composite is

234   highly enhanced, what should create a suitable surface chemistry, which could enable the

235   photocatalyst surface to the ERY adsorption (Krishnan et al., 2017).

236   **Figure 2.**

237

238   The surface electrical charge of TiO_2 and SnO_2-doped TiO_2 catalysts present positive values

239   in the same pH of the ADS and HP tests, as seen by the Zeta potential as a function of pH

240   (Kusior et al., 2019) Similarly, at this pH, ERY presents a pKa = 8.89 (Schafhauser et al., 2018).

241   This behavior negatively influences the approach and adsorption of ERY on the surface of these

242   catalysts due to electrostatic repulsion. In this work it was decided not to perform the correction or

243   to control the pH before and during testing in order to obtain results for natural pH values of ERY

244   in water.

245   The specific load results (Table 1) show that the M3 catalyst has the highest value among all

246   structured catalysts. The highest ADS value obtained by the M3 catalyst may also be related to its

247   higher specific load value, because a higher ADS of organic compounds is related to the mass of

248   catalyst (Kusior et al., 2019).

249   However, other characteristics of the surface, such as greater surface area and a reduction of

250   the grain boundary electron barrier (Krishnan et al., 2017), may be related to ERY ADS, because it

251   was observed that the M1 catalyst had a higher specific load value and lower ADS results than the

252   M2 and M3 catalysts.

253   As already shown in the literature, depending on the emission spectrum of the artificial

254   irradiation source (UV-A, UV-B or UV-C) and the energy of its photons, ERY can undergo DP,

255   mainly with sources of UV-C radiation (Franzen Ramos et al., 2020; Hassib et al., 2011). Aiming to

256   evaluate the possibility of ERY photolysis, tests were carried out in the reactor (Fig. 1) without

257   catalysts, using the 9 W UV-A lamp which emits 12 W m^{-2} at 365 nm (see supplementary material,

258   Fig. S2).

259   Fig. 2b shows that DP plays a discrete role in the ERY oxidation, contributing to 29 % and

260   13 % in degradation and mineralization, respectively. This finding can be associated to the low

261   absorbance of UV-A radiation by ERY, as ERY is considered a weakly absorbing macrolide

262   antibiotic (Hassib et al., 2011). Studies conducted by Franzen Ramos et al. (2020) and

263   Rattanapoltaveechai et al. (2007) showed that ERY presents a small peak of absorbance at 285 nm

264   (UV-C), far from the radiation emitted by the UV-A lamp used in this work. In fact, it is known that

265   only 3-5 % of the solar radiation reaching the earth surface is composed by UV-A

266   (Del Angel et al., 2018; Wei et al., 2018). Therefore, ERY degradation in natural environments is

267   difficult, being, for this reason, considered as a contaminant of high photodegradation difficulty

268   (Batchu et al., 2014; Fernández et al., 2019; Karaolia et al., 2018; Li et al., 2014;

269   Palmisano et al., 2015; Franzen Ramos et al., 2020; Voigt and Jaeger, 2017).

270   Fig. 2b and 2c showed that the commercial mesh (CM) catalyst presented similar

271   degradation and mineralization results to those found during the DP test. This result was not

272   expected, since the CM should be excited by UV-A irradiation, generating the e_{cb}^{-}/h_{vb}^{+} pairs, and,

273   as a consequence, radicals should be formed and act on the ERY oxidation. This infers that the

274 generation of the pair e_{cb}^-/h_{vb}^+ does not occur effectively, or that there are large electronic

275 recombination, leading to a lower ERY oxidation.

276 On the other hand, all prepared catalysts, with or without tin, showed better ERY oxidation

277 results than CM. Possible causes for the lower photocatalytic activity of this commercial catalyst

278 may be due to the composition of 70 % TiO_2 in the form of rutile, which has less photocatalytic

279 activity compared to the anatase form (Pelegrini et al., 2001). Another fact that can explain the

280 lower oxidation result is that TiO_2/RuO_2 catalysts are considered active catalysts, which means that

281 they have a strong interaction between the $HO^{\bullet}$ generated radical during photocatalysis and the

282 catalyst surface, which makes this radical less available for the oxidation of organic matter

283 (dos Santos et al., 2011).

284 The M1 catalyst (tin-free coverage) exhibited better results than the commercial mesh CM.

285 The possible explanation can be related to the higher TiO_2 load in M1 than in CM. Besides, the

286 TiO_2 source used in M1 is Degussa P25, a known catalyst that has a specific surface area of 50 m^2

287 g^{-1}, a proportion of the crystalline phase of 80 % anatase and 20 % rutile and a particle diameter of

288 21 nm. These properties turn Degussa P25 one of the most used catalysts. Other works conducted

289 by Trindade et al. (2018) and da Silva et al. (2016) have also shown that the catalysts prepared by

290 the washcoating method showed similar or better results when compared to the CM.

291 The prepared catalysts M2 and M3 presented better results than M1 for ERY degradation

292 and mineralization, what is associated to the presence of Sn in their composition. Doping TiO_2 with

293 other materials, such as metals, semiconductors or inorganic acids, aims to increase the lifetime of

294 the e_{cb}^-/h_{vb}^+ pair formed during the irradiation of the catalyst surface with UV or visible light, if the

295 component used in doping absorbs this radiation, thus allowing higher degradation of the

296 contaminants (Del Angel et al., 2018; Humayun et al., 2018; Kusior et al., 2019).

297 In this case, the titanium oxide doped with tin can result on the formation of a $Ti_{1-x}Sn_xO_2$

298 solid solution, leading to a lower internal recombination of the e_{cb}^-/h_{vb}^+ pairs and increasing the

299 photocatalytic activity (Kusior et al., 2019; Moniz et al., 2015). However, this improvement in

300 catalytic activity did not occur for catalysts M4 and M5 that also have tin in their composition.

301   Fig. 2b also shows an exponential decay, typical of pseudo-first order reactions, mainly for

302 the degradation of antibiotics (Franzen Ramos et al., 2020). Based on this assumption, the constants

303 were estimated for the first 60 min of reaction, using a well-known pseudo-first order equation to

304 estimate the kinetic constants presented in the inset on Fig. 2b. The results show that the M3

305 catalyst had the highest kinetic constant value, which indicates that the process occurred more

306 quickly in this structured catalyst compared to other ones, a behavior that may be linked to the type

307 II heterostructure formed (Kusior et al., 2019). The kinetic constant of the CM showed a lower

308 result than the DP process, which indicates that the photocatalytic processes did not occur

309 effectively, probably due the high presence of the rutile form.

310   Tin-doped titanium oxide can lead to the formation of three different types of

311 heterostructures, defined as the interfacial union of two or more components (Fig. 3) (Del Angel et

312 al., 2018), and only one of them leads to an improvement in the photocatalytic activity.

313   A type I heterostructure, or straddling gap, is formed by the junction of two components

314 where the conduction band of a component A presents greater energy, while presenting a valence

315 band with lower energy, when compared to the other component B (Del Angel et al., 2018; Moniz

316 et al., 2015). In this way the transfer of e_{cb}^-/h_{vb}^+ occurs from one component to the other, causing the

317 accumulation of these loads in only one of them (Moniz et al., 2015). This accumulation in only one

318 component, besides not decreasing the internal recombination rate, provides the accumulation of

319 charges in the component that has a lower redox potential, what significantly decreases the

320 formation of HO$^•$ during heterogeneous photocatalysis (Low et al., 2017).

321   At the type II heterostructure, or staggered gap, photoinduced charge separation effectively

322 occurs, since the lowest energy state for h_{vb}^+ may be on one side of the junction, whereas the lowest

323 energy for e_{cb}^- will be on the opposite side (Del Angel et al., 2018; Kusior et al., 2019). This

324 separation of charges provides increased lifetime of the loads generated, that, through chain

325 reactions, perform the degradation of organic compounds (Del Angel et al., 2018; Kusior et al.,

326 2019).

327   The type III heterostructure, or broken gap, occurs at the junction of two components with a

328 big difference between the components bands, which does not provide transfer of loads generated

329 between components to another (Kusior et al., 2019). This heterojunction is achieved when solid Z-

330 schemes are built (Del Angel et al., 2018).

331   The M3 behavior may be linked to the formation of heterojunction staggered gap (type II)

332 that increases the lifetime of the charges generated during the photocatalytic process (Fig. 3), by

333 allowing the transfer of e_{cb}^- from TiO_2 to SnO_2 and h_{vb}^+ from SnO_2 to TiO_2, diminishing internal

334 recombination (Kusior et al., 2019).

335   **Figure 3.**

336

337   The pH values did not vary significantly during the HP tests, with an average initial value of

338 5.4 ± 0.1 and a final one of 4.7 ± 0.2. This decrease in the pH values during the HP tests can be

339 associated to the formation of organic acids. Slightly acidic pH values (around 5) lead to better

340 mineralization of ERY, since most of the by-products generated during HP have a negative charge

341 in acidic pH solutions, what favors the adsorption on the positive surface of TiO_2 and TiO_2/SnO_2

342 catalysts (Fernandez et al., 2019; Li et al., 2014).

343

344 **3.2 Carboxylic acids generation**

345   Fig. 2b and 2c show a difference in removal values between degradation and mineralization,

346 suggesting that ERY oxidation occurs in more than one step. During the ERY photocatalysis, first

347 the cleavage of the $C - C$ bonds of the ERY molecule occurs, mainly by the action of the $HO_{ads}^\bullet$,

348 where, through the internal cyclization, the generation of by-products occurs, such as heterocyclic

349 compounds, aromatic esters and aliphatic tertiary amines (Llorca et al., 2015; Pérez et al., 2017).

350 These by-products then undergo catalytic degradation processes, also mainly due to the action of

351   HO•, leading to the production of low-molecular-weight organic acids (Llorca et al., 2015;

352   Pérez et al., 2017).

353   During the photocatalytic tests, the presence of formic (1 carbon), acetic (2 carbons) and

354   isovaleric (5 carbons) acids was not detected with any of the tested catalysts, as exhibited in Fig. 4.

355   However, an intense production of oxalic (2 carbons, Fig. 4a), propionic (3 carbons, Fig. 4b) and

356   tartaric (4 carbons, Fig. 4c) acids in the experiments carried out with all tested catalysts was

357   observed. The proportion value (in %) of each carboxylic acid was calculated by dividing the C/C_0

358   value divided by the sum of the C/C_0 values of all the carboxylic acids detected.

359   The generation of lower chain organic acids, such as formic (1 carbon), oxalic and acetic (2

360   carbons) and propionic (3 carbons) acids, indicates that one more step is necessary to lead to

361   mineralization (Serpone et al., 2005). On the other hand, the generation of tartaric (4 carbons) and

362   isovaleric (5 carbons), or higher chain acids, indicates that one more degradation step must be taken

363   to achieve the total mineralization, because acids with 4 or more carbons must be broken into

364   smaller acids (1-3 carbons) (Gandhi et al., 2012; Pérez et al., 2017; Serpone et al., 2005).

365   M5 and CM lead to the formation of organic acids and their degradation in smaller amounts,

366   when compared to the other catalysts (not shown). This result is expected, since M5 and CM

367   present lower ERY adsorption, degradation and mineralization (Fig. 2a, 2b and 2c, respectively).

368   **Figure 4.**

369

370   For all catalysts, except M3, a high generation of tartaric acid during the HP tests was found.

371   The production of carboxylic acid with 4 carbons may be linked to the lower generation of the HO•

372   by these catalysts, reducing the ERY oxidation until mineralization. The production profile of

373   tartaric acid during the HP evaluation with M3 was a typical for an intermediate product, having a

374   maximum between 5 – 15 min (Fig. 4d). The different behavior of the M3 catalyst, resulting in

375   lower production of carboxylic acids with more or equal 4 carbons, as well as in higher adsorption,

376   degradation and mineralization, may be associated to a successful formation of heterojunction type

377 II (Fig. 4). This structure would increase the lifetime of the e_{cb}^-/h_{vb}^+ pairs, favoring the ERY

378 oxidation by $HO^{\bullet}$ and $O_2^{-\bullet}$ generated at the M3 surface.

379

380 **3.3 Stability assessment**

381 After ADS and photocatalytic tests with all the prepared structured catalysts (M1, M2, M3,

382 M4 and M5) and with the commercial mesh (CM), it was found that M3 exhibited the best results,

383 resulting in 67 % of ERY degradation and 46 % of mineralization. Therefore, long-term tests were

384 performed with this catalyst. For this purpose, the tests were carried out in the same conditions that

385 the previously ones and in the same reactor (Fig. 1).

386 After 240 min (first test - Fig. 5a), 67 % and 47 % of ERY degradation and mineralization

387 were obtained, respectively. After 2280 min (twelfth test), a decrease of 50 % in the degradation

388 and 29 % in the mineralization of ERY was observed. This decrease may be related to the poisoning

389 of the catalyst surface, caused by the adsorption of by-products generated in the ERY

390 photocatalysis.

391 In a study conducted by da Silva et al. (2016), using a TiO_2-foam, a reduction in the

392 mineralization of nonylphenol ethoxylated was found after ten cycles (600 min), and it was caused

393 by the degradation by-products deposition on the catalyst surface. The photocatalytic activity was

394 restored after cleaning steps. Moreover, Mugunthan et al. (2019) studied the diclofenac degradation

395 over a TiO_2–SnO_2 catalyst and found a degradation reduction from 89 % to 53 % after 4 cycles

396 (1200 min). The authors attributed the poisoning effect to the accumulation of by-products on the

397 catalyst surface, which led to a decrease in the number of exposed active sites.

398 In order to try to restore the M3 catalytic activity, a cleaning step with a HNO_3 solution

399 (10% v.v) and with deionized water was performed after the twelfth test. Subsequently,

400 photocatalytic tests were carried out and the results are presented in Fig. 5a. These show that a great

401 part of the activity of M3 was restored (57 % in degradation and 37 % in mineralization), indicating

402 a high catalytic stability.

403 **Figure 5.**

404

405   To elucidate the behavior of the decrease in ERY degradation and mineralization found in

406 the long-term tests (Fig. 5a), the organic acids analysis was also performed. Fig. 5b shows that from

407 the sixth long-term test (1200 min) there is a decrease in the production of oxalic acid (2 carbons)

408 and an increase in the generation of tartaric acid (4 carbons), in relation to the proportion of the

409 analyzed acids. It is also noted, from the eleventh test (2400 min), the generation of formic (1

410 carbon), acetic (2 carbons) and isovaleric (5 carbons). The chromatograms of organic acids obtained

411 through HPLC are shown in Fig. S3 (see supplementary material, Figure S3).

412   The results presented in Fig. 5b corroborate those shown in Fig. 5a. A loss of the

413 photocatalytic activity of the M3 catalyst was observed. This may be related to the catalyst

414 detaching from the substrate or to the poisoning of its surface. These problems lead to a decrease in

415 the generation of $HO^{\bullet}$, and, as a direct consequence, to a higher production of organic acids, mainly

416 with 5 carbons; also to less mineralization. However, after a cleaning step with nitric acid solution

417 (10% v.v), the activity of the M3 catalyst was restored and formic, acetic and isovaleric acids were

418 no longer detected.

419   Based on all the obtained information on adsorption, degradation, mineralization and

420 formation of organic acids, a mechanism for charge transferring between TiO_2 and SnO_2, and the

421 corresponding generation of radicals and ERY degradation, was proposed in Fig. 6.

422   When the UV-A lamp is turned-on, there is photon absorption by TiO_2, and one electron

423 from the conduction band of TiO_2 is transferred to the conduction band of SnO_2 (presented in red

424 color). At the same time, h_{vb}^+ is transferred from the valence band of SnO_2 to the valence band of

425 TiO_2 (blue color). This charge transfer in the heterojunction staggered gap (type II), as shown in

426 Fig. 3, allows a decrease in the internal recombination (green color), favoring the generation of $HO^{\bullet}$

427 and $O_2^{-\bullet}$.

428   The generation of HO$^\bullet$, O$_2^{-\bullet}$ and h_{vb}^+ at the surface of the M3 catalyst leads to ERY

429   oxidation. Its degradation generates mainly oxalic and propionic acids and mineralization products

430   (CO$_2$, H$_2$O and inorganic ions).

431   **Figure 6.**

432

433   **3.4 Morphology and physicochemical characterization of the photocatalytic coatings**

434   The photocatalytic coatings morphologies are shown in Table 1. The coating of M1 (without

435   Sn) covered uniformly all the wire walls of the mesh, as was reported by Trindade et al. (2018). The

436   same morphology was observed on M2, M3 and M4, despite the Sn addition. However, the use of

437   SnO$_2$ nanoparticles (M5) had an undesirable effect on the coating morphology; some

438   agglomerations on the surface and wire intersections were generated and those could affect its

439   adherence. The coatings loadings, expressed as mg per cm^2 of wire, were quite similar for the five

440   structured catalysts, being these values between 4.2 and 4.9 mg cm^{-2}.

441   **Table 1**

442   Moreover, the elemental chemical composition of each Sn-Ti based coating was estimated

443   via SEM/EDS in different regions. The bulk Sn/Ti ratios and the average weight percentages of Sn

444   with their standard deviations (SD) are presented in Table 1. The Sn/Ti ratio of M2 resulted to be

445   the highest value obtained for these coatings as a consequence of the method used for the Sn

446   incorporation, which was a Sn oxalate impregnation. This procedure generated a high Sn loading

447   and a heterogeneous distribution over the coating, as indicated by its standard deviation. Therefore,

448   some regions with SnO$_2$ particles accumulations were generated on this structured catalyst.

449   Contrarily, the incorporation of SnO$_2$ in the washcoating suspension as microparticles (M4)

450   and nanoparticles (M5) drove to lower bulk Sn/Ti ratios and weight percentages of Sn (Table 1).

451   However, their standard deviations were high, indicating that the Sn distribution in those coatings

452   was not uniform.

453   On the other hand, when the washcoating suspension contained tin oxalate together with the

454   other components, the obtained coating (M3) presented a homogeneous distribution of Sn along the

455   coating wires, with a low SD of the Sn wt. % ($\pm$ 0.03%) and a Sn/Ti ratio of 0.025.

456   The weight composition of the CM catalyst is 21.5 % Ti and 18.3 % Ru (Table 2 and Fig.

457   S4 at supplementary material), being the atomic percentage 70 % Ti and 30 % Ru. The obtained

458   values were close to those reported by the manufacturer company (71.4 % Ti and 28.6 % Ru).

459

460   **Table 2**

461

462   After three reaction tests, the CM catalyst retained a high percentage in weight of carbon

463   (39.0 %), which can explain its lower catalytic activity compared to the Ti/Sn based catalysts.

464   The fresh M3 catalyst presented a tin weight percentage of 0.20 $\pm$ 0.03% on the coating

465   (Table 2). The presence of Sn in concentrations higher than 1.0 %, may not be beneficial for the

466   photocatalytic activity (Lin et al., 1999). When this Sn concentration is exceeded, Sn is not inserted

467   into Ti interstitial spaces, leading to the formation of free SnO_2. In this situation, the photocatalytic

468   activity will be impairing because SnO_2 has a larger bandgap than TiO_2. Besides, the type II

469   heterojunction between SnO_2 and TiO_2 will not be formed (Lin et al., 1999).

470   In addition, the deposition of organic content (presence of 9.05 % carbon) on the surface of

471   the M3 catalyst after all tests (more than 400 h) was measured (Table 2), confirming the results

472   found in Fig. 5a and 5b. The cleaning step of the M3 catalyst was successful in removing the

473   organic content present on its surface, therefore restoring its catalytic activity. However, the

474   catalytic activity recovery was not of 100 %. This fact can be linked to the presence of a 5.4 % of

475   iron (Table 2), which is a component of the AISI 304 stainless steel used as a substrate, indicating a

476   partial detaching of the catalyst anchored to the substrate surface.

477   The crystalline phases of the coatings were identified by XRD (Fig. 7). For all structured

478   catalysts (M1-M5), the main phase of TiO$_2$ was anatase (JCPDS Card n° 01-084-1285). However,

479   the contribution of TiO$_2$ in rutile (JCPDS Card n° 21-1276) form was also observed. Therefore,

480   after the washcoating procedure the TiO$_2$ phase structures remained as those of P25, as reported by

481   Trindade et al. 2018. The greater presence of anatase explains the higher activity of these catalysts

482   in relation to the CM catalyst Ti$_{0.7}$Ru$_{0.3}$O$_2$ – Ti, in which TiO$_2$ is under the rutile form, and that it

483   has less catalytic activity, due to greater internal recombination of e_{cb}^-/h_{vb}^+ pair (Babic et al., 2017).

484   In addition to the presence of TiO$_2$ in the rutile structure in the CM catalyst (Fig. 7), which has less

485   catalytic activity compared to the anatase form, carbon hinders the ability to generate radicals that

486   are characteristic of AOP processes. This suggests that the prepared structured catalysts (M1 to M5)

487   present better hydrodynamics and catalytic characteristics which result in less carbon accumulation

488   on the catalyst surface.

489   The diffraction signals of tetragonal ZrO$_2$ (JCPDS Card n° 79-1769) were also observed in

490   Figure 7. Nanoparticles of ZrO$_2$ were added in the washcoating suspension as binder in order to

491   increase the anchorage among the catalytic particles and the structured substrate surface (Trindade

492   et al., 2018). Furthermore, two small diffraction signals at 43.67° and 44.76°, attributed to γ-Fe

493   (JCPDS Card n° 00-006-0696) and α-Fe (JCPDS Card n° 01-087-0722), were distinguished in the

494   M2-M5 samples. These phases belong to the wire meshes used as substrates. Besides, no

495   diffractions associated to Sn species were observed. This absence is due to the small bulk

496   concentration of Sn species with respect to TiO$_2$ (Sn/Ti ratio: 0.012).

497   **Figure 7**

498   To evaluate the formation of the Ti$_{1-x}$Sn$_x$O$_2$ solid solution the XRD results were used to

499   calculate the lattice constants (a, b and c), unit cell volume and interplanar distance (Miller index

500   101) of the TiO$_2$ anatase, the main form of TiO$_2$ in the M1-M5 photocatalysts. To calculate the

501   lattices values of the structured photocatalysts, the Bragg equation was used and compared with the

502   TiO$_2$ anatase (JCPDS Card n° 01-084-1285) and cassiterite SnO$_2$ (JCPDS Card n° 00-041-1445)

503 values (Yang et al., 2011). Table 3 shows the lattice values, unit cell volume and interplanar

504 distance for each structured photocatalyst, pure TiO_2 anatase and pure SnO_2 (Miller index 111).

505 **Table 3**

506   An increase in the values of the lattice constants, unit cell volume and interplanar distance

507 for the structured photocatalyst M3 in relation to the structured photocatalyst M1 (without Sn) and

508 to TiO_2 pure anatase was observed (Table 3). This increase in the lattice constants of TiO_2 anatase

509 suggests that some Ti^{4+} is replaced by Sn^{4+} in the crystalline network of the TiO_2 anatase phase

510 (Yang et al., 2019). This substitution induced the effective formation of a $Ti_{1-x}Sn_xO_2$ solid solution

511 in M3 (Yang et al., 2019, Chen et al., 2013). For the other structured photocatalysts (M2, M4 and

512 M5) there were no significant changes in the values of the constant lattices and interplanar distances

513 in relation to M1 (without Sn) and TiO_2, which indicates that in these photocatalyst structures the

514 formation of $Ti_{1-x}Sn_xO_2$ solid solution does not occur. Thus, the incorporation of Sn oxalate to the

515 washcoating suspension favors the insertion of Sn^{4+} in the TiO_2 structure.

516   The Sn-containing photocatalytic coatings obtained in this work presented crystallite sizes

517 higher than that of M1 (Table 3). Maver et al. reported a similar effect on Ti-Sn samples prepared

518 by the sol-gel method. The authors observed that at low Sn loadings the calcination process

519 promoted the formation of larger crystallites of the crystalline phases, while at higher Sn contents

520 this behavior was not verified (Maver et. al 2020).

521   Table 4 displays the obtained surface data for the Sn-doped structured photocatalysts. The

522 Ti 2p, Zr 3d, Sn 3d and O 1s regions were analyzed. In anatase bulk TiO_2 the Ti $2p_{3/2}$ and Ti $2p_{1/2}$

523 peaks appear at 458.7 – 458.9 eV and 464.4 – 464.6 eV, respectively, indicating Ti^{4+} in TiO_2

524 (Mahy et al., 2019; Mintcheva et al., 2019). In the case of the Sn-doped photocatalysts the peaks

525 were shifted to lower binding energies – BEs – (458.4 – 458.5 eV), which could indicate a partial

526 reduction of Ti^{4+} to Ti^{3+} and is associated to the presence of oxygen vacancies at the surface of

527 these Sn-doped catalysts (Toloman et al., 2019; Zhao et al., 2020; Yang et al., 2019). Particularly,

528   the Ti $2p_{3/2}$ peak for M4, whose Sn source was powder SnO_2, was very close to that of pure TiO_2,

529   inferring that this method did not induce changes in the Ti surface environment. On the other hand,

530   the Zr $3d_{5/2}$ signal in all Sn-doped structured catalysts was found to be $182.0 - 182.1$ eV, practically

531   equal for all doped structured catalysts, with a spin-orbit splitting of 2.4 eV, characteristic of Zr^{4+} in

532   ZrO_2

533   (Bronsato et al., 2020; Liu et al., 2019). The fact that the BEs of these catalytic systems were almost

534   the same for Zr but slightly different for Ti suggests that Sn incorporation affected the Ti surface

535   environment but not the Zr environment.

536   Some changes in the surface were also observed by the analysis of the Sn 3d region. Bulk

537   SnO_2 presents its Sn $3d_{5/2}$ peak at $486.7 - 487.0$ eV with a spin-orbit splitting of 8.4 eV

538   (Um et al. 2019). This peak was found at lower BEs than that of bulk SnO_2, $486.2 - 486.3$ eV, for

539   M2, M3 and M5. This shift to lower binding energies is due to the higher electronegativity of Sn

540   compared to Ti (Um et al. 2019; Duan et al., 2012). Furthermore, this value was very close to bulk

541   SnO_2 for M4, as it was the case with the Ti analysis. These results indicate that in M4 the

542   interaction between Sn and Ti is very weak. Also, all the catalysts presented a small shoulder at ~

543     $484 - 485$ eV, assigned to Sn^{2+} species (Toloman et al., 2019, Bjelajac et al., 2020).

544   Additionally, the O 1s region was investigated in order to study the surface oxygen species

545   associated with oxygen vacancies. It is reported in the literature that changes induced in TiO_2, i. e.

546   Sn doping, can lead to the generation of defects in this compound associated to oxygen vacancies

547   (Zhao et al., 2020; Yang et al., 2019). Furthermore, several publications reported that oxygen

548   vacancies promote the reduction of the electron-hole pairs recombination and therefore enhance the

549   photocatalytic degradation performance for organic pollutants (Zhao et al., 2020, Li et al., 2016;

550   Tian et al. 2018). All Sn-doped O 1s spectra revealed two oxygen species: $529.7 - 529.9$ eV,

551   associated to crystal lattice oxygen (O_L), and $531.6 - 531.9$ eV attributed to absorbed oxygen

552   species (O_V, oxygen vacancies) [4,12]. The O_V/O_L ratios were obtained for the Sn-doped structured

553   catalysts and it was found that this value was the highest for M3 (0.17), slightly lower for M2 (0.15)

554 and lower for M4 and M5 (0.11 and 0.12 respectively), in close agreement with their respective

555 photocatalytic performances (Fig. 2).

556 **Table 4**

557

4   CONCLUSIONS

The degradation of ERY by heterogeneous photocatalysis was investigated using a series of TiO_2 and $Ti_{1-x}Sn_xO_2$ catalysts prepared by the washcoating method. Tests of adsorption, degradation and mineralization of ERY were done and the production of carboxylic acids was evaluated. Long-term tests and physicochemical characterization were carried out. A scheme demonstrating the formation of the heterojunction, its electron transfer, generation of radicals and the route of degradation and mineralization of ERY was also proposed.

It was found that the order and type of Sn sources incorporated in the synthesis procedure affect the catalytic activity due to the formation of a solid solution with different type of heterostructures. An improvement in the catalytic properties was associated to the incorporation of tin into the titanium oxide matrix, which takes place in the M3 structured system. The characterization of this structured system suggested the Ti-Sn-O solid solution formation, due to the utilization of tin oxalate for the generation of the catalytic film. This fact is also coupled with its morphological features such as the staggered gap (type II) formation and with the optimized titanium to tin molar ratio. In this situation, there is a better separation of the electron/hole pairs, favoring the generation of hydroxyl radicals and the ERY oxidation.

The long-term tests showed a loss of catalytic activity which was related to the presence of organic compounds and to a partial loss of catalytic material. Nevertheless, after a cleaning step, the activity of the catalyst was almost completely restored. In fact, the catalyst with better results in terms of ERY degradation and mineralization (M3) showed high stability in long-term tests up to 3360 min. The obtained results show the possible use of Ti-Sn structured photocatalysts for water and wastewater treatment.

584 CAPG-BA 73/14 and UNL (CAI+D 50020150100081LI) from Argentina and from the Ibero-

585 American Program on Science and Technology for Development (CYTED).

586

587 **REFERENCES**

588 Aldon, L., Kubiak, P., Picard, A., Jumas, J.C., Olivier-Fourcade, J., 2006. Size Particle Effects on
589 Lithium Insertion into Sn-doped TiO2Anatase. Chem. Mater. 18, 1401-1406.
590 http://dx.doi.org/10.1021/cm051445v.

591 Andreozzi, R., Caprio, V., Insola, A., Marotta, R., 1999. Advanced oxidation processes (AOP) for
592 water purification and recovery. Catal. Today 53, 51–59. https://doi.org/10.1016/S0920-
593 5861(99)00102-9

594 Ayoub, H., Roques-Carmes, T., Potier, O., Koubaissy, B., Pontvianne, S., Lenouvel, A., Guignard,
595 C., Mousset, E., Poirot, H., Toufaily, J., Hamieh, T., 2019. Comparison of the removal of 21
596 micropollutants at actual concentration from river water using photocatalysis and photo-Fenton. SN
597 Appl. Sci. 1, 1–12. https://doi.org/10.1007/s42452-019-0848-y

598 Babić, S., Ćurković, L., Ljubas, D., Čizmić, M., 2017. TiO2 assisted photocatalytic degradation of
599 macrolide antibiotics. Curr. Opin. Green Sustain. Chem. 6, 34–41.
600 https://doi.org/10.1016/j.cogsc.2017.05.004

601 Barrios-Estrada, C., de Jesús Rostro-Alanis, M., Muñoz-Gutiérrez, B.D., Iqbal, H.M.N., Kannan, S.,
602 Parra-Saldívar, R., 2018. Emergent contaminants: Endocrine disruptors and their laccase-assisted
603 degradation – A review. Sci. Total Environ. 612, 1516–1531.
604 https://doi.org/10.1016/j.scitotenv.2017.09.013

605 Bartelt-Hunt, S., Snow, D.D., Damon-Powell, T., Miesbach, D., 2011. Occurrence of steroid
606 hormones and antibiotics in shallow groundwater impacted by livestock waste control facilities. J.
607 Contam. Hydrol. 123, 94–103. https://doi.org/10.1016/j.jconhyd.2010.12.010

608 Bedner, M., MacCrehan, W.A., 2006. Transformation of acetaminophen by chlorination produces
609 the toxicants 1,4-benzoquinone and N-acetyl-p-benzoquinone imine. Environ. Sci. Technol. 40,
610 516–522. https://doi.org/10.1021/es0509073

611 Bjelajac, A., Petrović, R., Vujancevic, J., Veltruska, K., Matolin, V., Siketic, Z., Provatas, G.,
612 Jaksic, M., Stan, G.E., Socol, G., Mihailescu, I.N., Janaćković, D. 2020. Sn-doped TiO2
613 nanotubular thin film for photocatalytic degradation of methyl orange dye. J. Phys. Chem. Solids.
614 147, 109609. https://doi.org/10.1016/j.jpcs.2020.109609

615 Bronsato, B.J.S., Zonetti, P.C., Moreira, C.R., Mendonza, C.D., da Costa, M.E.H.M., Alves, O.C.,
616 de Avillez, R.R. Appel, L.G. 2020. How the interaction between In2O3-ZrO2 promotes the
617 isobutene synthesis from ethanol? Catal. Today. https://doi.org/10.1016/j.cattod.2020.07.004

618 Bush, K., 2010. Antimicrobial Agents. Semin. Dial. 23, 472–474. https://doi.org/10.1111/j.1525-
619 139X.2010.00774.x

620 Byrne, C., Moran, L., Hermosilla, D., Merayo, N.,Blanco, Á., Rhatigan, S., Hinder, S.,Ganguly, P.,
621 Nolan, M., Pillai, S.C. Effect of Cu doping on the anatase-to-rutile phase transition in TiO2
622 photocatalysts : Theory and experiments, Appl. Catal. B Environ. 246 (2019) 266–276.
623 https://doi.org/10.1016/j.apcatb.2019.01.058.

624 Chen, Y.C., Hung, T.F., Hu, C.W., Chiang, C.Y., Huang, C.W., Su, H.C., Liu, R.S., Lee, C.H.,
625 Chang, C.C., 2013. Rutile-type (Ti,Sn)O2 nanorods as efficient anode materials toward its lithium
626 storage capabilities. Nanoscale. 5, 2254-2258. http://dx.doi.org/10.1039/c3nr33250k.

627 Choi, W., Termin, A., Hoffmann, M.R., 1994. The role of metal ion dopants in quantum-sized
628 TiO2: Correlation between photoreactivity and charge carrier recombination dynamics. J. Phys.
629 Chem. 98, 13669–13679. https://doi.org/10.1021/j100102a038

630 Da Silva, S.W., Bortolozzi, J.P., Banús, E.D., Bernardes, A.M., Ulla, M.A., 2016. TiO2 thick films
631 supported on stainless steel foams and their photoactivity in the nonylphenol ethoxylate
632 mineralization. Chem. Eng. J. 283, 1264–1272. https://doi.org/10.1016/j.cej.2015.08.057

633 Del Angel, R., Durán-Álvarez, J.C., Zanella, R., 2018. TiO2-Low Band Gap Semiconductor
634 Heterostructures for Water Treatment Using Sunlight-Driven Photocatalysis. Titan. Dioxide -
635 Mater. a Sustain. Environ. https://doi.org/10.5772/intechopen.76501

636 Dos Santos, I.D., Afonso, J.C., Dutra, A.J.B., 2011. Electrooxidation of phenol on a Ti/RuO2
637 anode: Effect of some electrolysis parameters. J. Braz. Chem. Soc. 22, 875–883.
638 https://doi.org/10.1590/S0103-50532011000500009

639 Duan, Y., Fu, N., Liu, Q., Fang, Y., Zhou, X., Zhang, J., Lin, Y. 2012. Sn-Doped TiO2 Photoanode
640 for Dye-Sensitized Solar Cells. J. Phys. Chem. 116, 8888 – 8893. https://doi.org/10.1021/jp212517k
641 European Commission., 2017. Study on the review of the list of Critical Raw Materials: Criticality
642 Assessments. Brussels. http://hytechcycling.eu/wp-content/uploads/Study-on-the-review-of-the-list-
643 of-Critical-Raw-Materials.pdf (accessed 18 May 2020).

644 Franzen Ramos, L., da Silva, S.W., Schneider, D.E., Rodrigues, M.A.S., Bernardes, A.M., 2020.
645 Mineralization of erythromycin by UV-based and electro-oxidation processes. J. Water Process
646 Eng. 33, 101039. https://doi.org/10.1016/j.jwpe.2019.101039

647 Gandhi, V., Mishra, M., Joshi, P.A., 2012. Titanium dioxide catalyzed photocatalytic degradation of
648 carboxylic acids from waste water: A review. Mater. Sci. Forum 712, 175–189.
649 https://doi.org/10.4028/www.scientific.net/MSF.712.175

650 Gaya, U.I., Abdullah, A.H., 2008. Heterogeneous photocatalytic degradation of organic
651 contaminants over titanium dioxide: A review of fundamentals, progress and problems. J.
652 Photochem. Photobiol. C Photochem. Rev. 9, 1–12.
653 https://doi.org/10.1016/j.jphotochemrev.2007.12.003

654 Gogoi, A., Mazumder, P., Tyagi, V.K., Tushara Chaminda, G.G., An, A.K., Kumar, M., 2018.
655 Occurrence and fate of emerging contaminants in water environment: A review. Groundw. Sustain.
656 Dev. 6, 169–180. https://doi.org/10.1016/j.gsd.2017.12.009

657 Hapeshi, E., Gros, M., Lopez-Serna, R., Boleda, M.R., Ventura, F., Petrovic, M., Barceló, D., Fatta-
658 Kassinos, D., 2015. Licit and Illicit Drugs in Urban Wastewater in Cyprus. Clean - Soil, Air, Water
659 43, 1272–1278. https://doi.org/10.1002/clen.201400483

660 Hassib, S.T., Farag, A.E., Elkady, E.F., 2011. Liquid chromatographic and spectrophotometric
661 methods for the determination of erythromycin stearate and trimethoprim in tablets. Bull. Fac.
662 Pharmacy, Cairo Univ. 49, 81–89. https://doi.org/10.1016/j.bfopcu.2011.07.008

663 Humayun, M., Raziq, F., Khan, A., Luo, W., 2018. Modification strategies of TiO2 for potential
664 applications in photocatalysis: A critical review. Green Chem. Lett. Rev. 11, 86–102.
665 https://doi.org/10.1080/17518253.2018.1440324

666 Kanakaraju, D., Glass, B.D., Oelgemöller, M., 2018. Advanced oxidation process-mediated
667 removal of pharmaceuticals from water: A review. J. Environ. Manage. 219, 189–207.
668 https://doi.org/10.1016/j.jenvman.2018.04.103

669 Karaolia, P., Michael-Kordatou, I., Hapeshi, E., Drosou, C., Bertakis, Y., Christofilos, D., Armatas,
670 G.S., Sygellou, L., Schwartz, T., Xekoukoulotakis, N.P., Fatta-Kassinos, D., 2018. Removal of
671 antibiotics, antibiotic-resistant bacteria and their associated genes by graphene-based TiO2

composite photocatalysts under solar radiation in urban wastewaters. Appl. Catal. B Environ. 224, 810–824. https://doi.org/10.1016/j.apcatb.2017.11.020

Konstantinou, I.K., Albanis, T.A., 2004. TiO2-assisted photocatalytic degradation of azo dyes in aqueous solution: Kinetic and mechanistic investigations: A review. Appl. Catal. B Environ. 49, 1–14. https://doi.org/10.1016/j.apcatb.2003.11.010

Krishnan, V.G., Elango, P., Purushothaman, A., Chandra Bose, A., 2017. Automated nebulizer sprayed tin doped titanium dioxide (SnxTi1-xO2) anatase nanofilms properties, gas sensing performance. Mater. Chem. Phys. 199, 113–121. https://doi.org/10.1016/j.matchemphys.2017.06.052

Kusior, A., Zych, L., Zakrzewska, K., Radecka, M., 2019. Photocatalytic activity of TiO2/SnO2 nanostructures with controlled dimensionality/complexity. Appl. Surf. Sci. 471, 973–985. https://doi.org/10.1016/j.apsusc.2018.11.226

Li, J., Xu, X., Liu, X., Yu, C., Yan, D., Sun, Z., Pan, L. 2016. Sn doped TiO2 nanotube with oxygen vacancy for highly efficient visible light photocatalysis. J. Alloy Compd. 679, 454-462. https://doi.org/10.1016/j.jallcom.2016.04.080

Li, Z., Li, M., Liu, X., Ma, Y., Wu, M., 2014. Identification of priority organic compounds in groundwater recharge of China. Sci. Total Environ. 493, 481–486. https://doi.org/10.1016/j.scitotenv.2014.06.005

Lin, A.Y.C., Tsai, Y.T., 2009. Occurrence of pharmaceuticals in Taiwan's surface waters: Impact of waste streams from hospitals and pharmaceutical production facilities. Sci. Total Environ. 407, 3793–3802. https://doi.org/10.1016/j.scitotenv.2009.03.009

Lin, J., Yu, J.C., Lo, D., Lam, S.K., 1999. Photocatalytic activity of rutile Ti1-xSnxO2 solid solutions. J. Catal. 183, 368–372. https://doi.org/10.1006/jcat.1999.2409

Lin, Y.C., Lai, W.W.P., Tung, H. hsin, Lin, A.Y.C., 2015. Occurrence of pharmaceuticals, hormones, and perfluorinated compounds in groundwater in Taiwan. Environ. Monit. Assess. 187. https://doi.org/10.1007/s10661-015-4497-3

Liu, J., Yang, H., Ren, B., Rong, Y., Xi, X. Lu, Y., Zhao, Y., Yang, J. 2019. Highly porous ZrO2 cellular ceramics with 3D network architecture. Ceram. Int. https://doi.org/10.1016/j.ceramint.2019.11.207

Llorca, M., Rodríguez-Mozaz, S., Couillerot, O., Panigoni, K., de Gunzburg, J., Bayer, S., Czaja, R., Barceló, D., 2015. Identification of new transformation products during enzymatic treatment of tetracycline and erythromycin antibiotics at laboratory scale by an on-line turbulent flow liquid-chromatography coupled to a high-resolution mass spectrometer LTQ-Orbitrap. Chemosphere 119, 90–98. https://doi.org/10.1016/j.chemosphere.2014.05.072

Low, J., Yu, J., Jaroniec, M., Wageh, S., Al-Ghamdi, A.A., 2017. Heterojunction Photocatalysts. Adv. Mater. 29, 1–20. https://doi.org/10.1002/adma.201601694

Mahy, J.G, Lambert, D.S., Tilkin, G.R., Wolfs, C., Poelman, D., Devred, F., Gaigneaux, E.M., Douven, S. 2019. Ambient temperature ZrO2-doped TiO2 crystalline photocatalysts: Highly efficient powders and films for water depollution. Mater. Today Energy. 13, 312 – 322. https://doi.org/10.1016/j.mtener.2019.06.010

Maver, K., Arčon, I., Fanetti, M., Emin, S., Valant, M., Štangar, U.L. 2020, Improved photocatalytic activity of anatase-rutile nanocomposites induced by low-temperature sol-gel Sn-modification of TiO2. Catal. Today. In Press. https://doi.org/10.1016/j.cattod.2020.01.045

Mintcheva, N., Srinivasan, P., Rayappan, J.B.B., Kuchmizhakd, A.A., Gurbatovd, S., Kulinich, S.A. 2020. Room-temperature gas sensing of laser-modified anatase TiO2 decoratedwith Au nanoparticles. Appl. Surf. Sci. 507, 145169. https://doi.org/10.1016/j.apsusc.2019.145169.

718 Mugunthan, E., Saidutta, M.B., Jagadeeshbabu, P.E., 2019. Photocatalytic degradation of diclofenac
719 using TiO2–SnO2 mixed oxide catalysts. Environ. Technol. 40, 929–941.
720 https://doi.org/10.1080/09593330.2017.1411398

721 Palmisano, R., Campanella, L., 2015. Photo-Degradation of Amoxicillin, Streptomycin,
722 Erythromycin and Ciprofloxacin by UV and UV/TiO2 Processes. Evaluation of Toxicity Changes
723 Using a Respirometric Biosensor. J. Environ. Anal. Chem. 02. https://doi.org/10.4172/2380-
724 2391.1000143

725 Patel, M., Kumar, R., Kishor, K., Mlsna, T., Pittman, C.U., Mohan, D., 2019. Pharmaceuticals of
726 emerging concern in aquatic systems: Chemistry, occurrence, effects, and removal methods. Chem.
727 Rev. 119, 3510–3673. https://doi.org/10.1021/acs.chemrev.8b00299

728 Pelegrini, R.T., Freire, R.S., Duran, N., Bertazzoli, R., 2001. Photoassisted electrochemical
729 degradation of organic pollutants on a DSA type oxide electrode: Process test for a phenol synthetic
730 solution and its application for the E1 bleach Kraft mill effluent. Environ. Sci. Technol. 35, 2849–
731 2853. https://doi.org/10.1021/es001784j

732 Pérez, T., Sirés, I., Brillas, E., Nava, J.L., 2017. Solar photoelectro-Fenton flow plant modeling for
733 the degradation of the antibiotic erythromycin in sulfate medium. Electrochim. Acta 228, 45–56.
734 https://doi.org/10.1016/j.electacta.2017.01.047

735 Pesci, F.M., Wang, G., Klug, D.R., Li, Y., Cowan, A.J., 2013. Efficient suppression of electron-
736 hole recombination in oxygen-deficient hydrogen-treated TiO2 nanowires for photoelectrochemical
737 water splitting. J. Phys. Chem. C 117, 25837–25844. https://doi.org/10.1021/jp4099914

738 Pico, Y., Belenguer, V., Corcellas, C., Diaz-Cruz, M.S., Eljarrat, E., Farré, M., Gago-Ferrero, P.,
739 Huerta, B., Navarro-Ortega, A., Petrovic, M., Rodríguez-Mozaz, S., Sabater, L., Santín, G.,
740 Barcelo, D., 2019. Contaminants of emerging concern in freshwater fish from four Spanish Rivers.
741 Sci. Total Environ. 659, 1186–1198. https://doi.org/10.1016/j.scitotenv.2018.12.366

742 Rodriguez-Narvaez, O.M., Peralta-Hernandez, J.M., Goonetilleke, A., Bandala, E.R., 2017.
743 Treatment technologies for emerging contaminants in water: A review. Chem. Eng. J. 323, 361–
744 380. https://doi.org/10.1016/j.cej.2017.04.106

745 Rui, Z., Wu, S., Peng, C., Ji, H., 2014. Comparison of TiO2 Degussa P25 with anatase and rutile
746 crystalline phases for methane combustion. Chem. Eng. J. 243, 254–264.
747 https://doi.org/10.1016/j.cej.2014.01.010

748 Sangchay, W., 2016. The Self-cleaning and Photocatalytic Properties of TiO2 Doped with SnO2
749 Thin Films Preparation by Sol-gel Method. Energy Procedia 89, 170–176.
750 https://doi.org/10.1016/j.egypro.2016.05.023

751 Schafhauser, B.H., Kristofco, L.A., de Oliveira, C.M.R., Brooks, B.W., 2018. Global review and
752 analysis of erythromycin in the environment: Occurrence, bioaccumulation and antibiotic resistance
753 hazards. Environ. Pollut. 238, 440–451. https://doi.org/10.1016/j.envpol.2018.03.052

754 Serpone, N., Martin, J., Horikoshi, S., Hidaka, H., 2005. Photocatalyzed oxidation and
755 mineralization of C1-C5 linear aliphatic acids in UV-irradiated aqueous titania dispersions-kinetics,
756 identification of intermediates and quantum yields. J. Photochem. Photobiol. A Chem. 169, 235–
757 251. https://doi.org/10.1016/j.jphotochem.2004.07.001

758 Shen, S., Chen, J., Wang, M., Sheng, X., Chen, X., Feng, X., Mao, S.S., 2018. Titanium dioxide
759 nanostructures for photoelectrochemical applications. Prog. Mater. Sci. 98, 299–385.
760 https://doi.org/10.1016/j.pmatsci.2018.07.006

761 Solís-Casados, D.A., Escobar-Alarcón, L., Gómez-Oliván, L.M., Haro-Poniatowski, E., Klimova,
762 T., 2017. Photodegradation of pharmaceutical drugs using Sn-modified TiO2 powders under visible
763 light irradiation. Fuel 198, 3–10. https://doi.org/10.1016/j.fuel.2017.01.059

Stackelberg, P.E., Gibs, J., Furlong, E.T., Meyer, M.T., Zaugg, S.D., Lippincott, R.L., 2007. Efficiency of conventional drinking-water-treatment processes in removal of pharmaceuticals and other organic compounds. Sci. Total Environ. 377, 255–272. https://doi.org/10.1016/j.scitotenv.2007.01.095

Thomas, J.M. Thomas, W.J., 2015. Principles and Practice of Heterogeneous Catalysis, second ed. Weinhein, VCH.

Tian, Q., Wei, W., Dai, J., Sun, Q., Zhuang, J., Zheng, Y., Liu, P., Fan, M., Chen, L. 2018. Porous Core-Shell TixSn1-xO2 Solid Solutions with Broad-light Response: One-pot Synthesis and Ultrahigh Photooxidation Performance. Appl. Catal. B, 244, 45-55. https://doi.org/10.1016/j.apcatb.2018.11.045

Toloman, D., Pana, O., Stefan, M., Popa, A., Leostean, C., Macavei, S. 2019. Photocatalytic activity of SnO2-TiO2 composite nanoparticles modified with PVP. J. Colloid Interface Sci. 542, 296 – 307. https://doi.org/10.1016/j.jcis.2019.02.026

Tong, L., Huang, S., Wang, Y., Liu, H., Li, M., 2014. Occurrence of antibiotics in the aquatic environment of Jianghan Plain, central China. Sci. Total Environ. 497–498, 180–187. https://doi.org/10.1016/j.scitotenv.2014.07.068

Trindade, C. de M., da Silva, S.W., Bortolozzi, J.P., Banús, E.D., Bernardes, A.M., Ulla, M.A., 2018. Synthesis and characterization of TiO 2 films onto AISI 304 metallic meshes and their application in the decomposition of the endocrine-disrupting alkylphenolic chemicals. Appl. Surf. Sci. 457, 644–654. https://doi.org/10.1016/j.apsusc.2018.06.287

Um, J.H., Lim, J., Hengge, K., Scheu, C., Yoon, W.S., Leed, J.K., Sung, Y.E. 2019. Pore-interconnected hollow (Sn,Ti)O2 solid-solution nanoparticles for lithium-ion battery anode materials. Compos. B. 166, 613 – 620. https://doi.org/10.1016/j.compositesb.2019.02.063

Vignesh, K., Rajarajan, M., Suganthi, A., 2014. Photocatalytic degradation of erythromycin under visible light by zinc phthalocyanine-modified titania nanoparticles. Mater. Sci. Semicond. Process. 23, 98–103. https://doi.org/10.1016/j.mssp.2014.02.050

Voigt, M., Jaeger, M., 2017. On the photodegradation of azithromycin, erythromycin and tylosin and their transformation products – A kinetic study. Sustain. Chem. Pharm. 5, 131–140. https://doi.org/10.1016/j.scp.2016.12.001

Westerhoff, P., Yoon, Y., Snyder, S., Wert, E., 2005. Fate of endocrine-disruptor, pharmaceutical, and personal care product chemicals during simulated drinking water treatment processes. Environ. Sci. Technol. 39, 6649–6663. https://doi.org/10.1021/es0484799

Xekoukoulotakis, N.P., Xinidis, N., Chroni, M., Mantzavinos, D., Venieri, D., Hapeshi, E., Fatta-Kassinos, D., 2010. UV-A/TiO2 photocatalytic decomposition of erythromycin in water: Factors affecting mineralization and antibiotic activity. Catal. Today 151, 29–33. https://doi.org/10.1016/j.cattod.2010.01.040

Yang, Y., Hu, C.C., Hua, C.C., 2011. Preparation and characterization of nanocrystalline TixSn1−xO2 solid solutions via a microwave-assisted hydrothermal synthesis process. CrystEngComm. 13, 5638–5641. http://dx.doi.org/10.1039/c1ce05353a.

Yang, Y., Li, H., Zhao, H., Qu, R., Zhang, S., Hu, W., Yu, X., Zhu, X., Liu, S., Zheng, C., Gao, X. 2019. Structure and crystal phase transition effect of Sn doping on anatase TiO2 for dichloromethane decomposition. J. Hazard. Mater. 371, 156 – 164. https://doi.org/10.1016/j.jhazmat.2019.02.103

Yang, Y., Ok, Y.S., Kim, K.H., Kwon, E.E., Tsang, Y.F., 2017. Occurrences and removal of pharmaceuticals and personal care products (PPCPs) in drinking water and water/sewage treatment plants: A review. Sci. Total Environ. 596–597, 303–320. https://doi.org/10.1016/j.scitotenv.2017.04.102

811 Yu, J., Wang, Y., Xiao, W., 2013. Enhanced photoelectrocatalytic performance of SnO2/TiO 2
812 rutile composite films. J. Mater. Chem. A 1, 10727–10735. https://doi.org/10.1039/c3ta12218b

813 Zhao, C., Yang, Y., Luo, L., Shao, S., Zhou, Y., Shao, Y., Zhan, F., Yang, J., Zhou, Y. 2018. γ-ray
814 induced formation of oxygen vacancies and Ti3+ defects in anatase TiO2 for efficient
815 photocatalytic organic pollutant degradation. Sci. Total Environ. In Press.
816 https://doi.org/10.1016/j.scitotenv.2020.141533.
817 Zhou, D., Chen, Z., Yang, Q., Shen, C., Tang, G., Zhao, S., Zhang, J., Chen, D., Wei, Q., Dong, X.,
818 2016. Facile Construction of g-C3N4Nanosheets/TiO2Nanotube Arrays as Z-Scheme Photocatalyst
819 with Enhanced Visible-Light Performance. ChemCatChem 8, 3064–3073.
820 https://doi.org/10.1002/cctc.201600828

Fig. 1. Scheme of the photocatalytic reaction system, where 1 is the non-irradiated reservoir, 2 is the photocatalytic reactor and 3 is the peristaltic pump (Masterflex® L/S® Easy-Load®).

Fig. 2. Evaluation of the prepared catalysts M1, M2, M3, M4, M5 and commercial one (CM) on ERY **(a)** adsorption, **(b)** degradation and **(c)** mineralization. Experimental conditions: ERY = 50 mg L^{-1}, pH = 5.4 at room temperature.

Fig. 3. Scheme of electron transfer principle from (A) SnO$_2$ into (B) TiO$_2$ **(a)** straddling gap (type I), **(b)** staggered gap (type II) and **(c)** broken gap (type III).

Fig. 4. Short carboxylic acids detected during photocatalytic evaluation for all catalysts. Where **(a)** is oxalic acid , **(b)** is propionic acid and **(c)** is tartaric acid. The profile of the short carboxylic acids generated and consumed during the photocatalytic test for the M3 catalyst are presented in **(d)**. Experimental conditions: ERY = 50 mg L^{-1}, pH = 5,4 and room temperature.

Fig. 5. M3 long-term photocatalytic tests before (0 – 2880 min) and after cleaning step (2880 – 3360 min) for **(a)** degradation and mineralization and **(b)** short carboxylic acid proportion of propionic (in red), tartaric (in green), oxalic (in pink), isovaleric (in orange), acetic (in magenta) and propionic (in blue) acids during the M3 long-term tests. Last 2 tests were carried out after cleaning the photocatalyst with HNO$_3$. Experimental conditions: ERY = 50 mg L^{-1}, pH = 5.4 and room temperature.

Fig. 6. Possible heterojunction staggered gap (type II) scheme formed between TiO$_2$ and SnO$_2$ in the prepared catalysts M3, and its action in the ERY oxidation. Adapted from Moniz *et al.* (2015).

Fig. 7. X-Ray difractograms for the structured catalysts, the commercial one, SnO$_2$ and TiO$_2$ Degussa P25. Symbols: ■ TiO$_2$ – Rutile, ▲ TiO$_2$ – Anatase, ● ZrO$_2$ – Tetragonal, ◆ SnO$_2$, ◀ γ-Fe, ▶ α-Fe.

Table 1. Morphology and loadings of the M1 to M5 structured photocatalysts and physicochemical characterization of the SnO_2-TiO_2 based photocatalytic coatings.
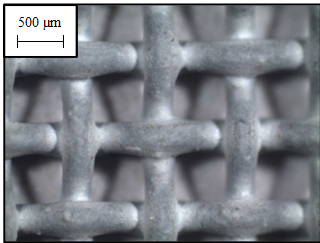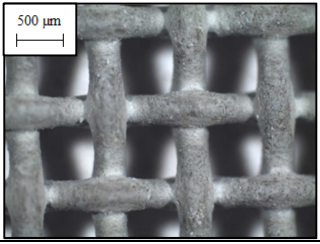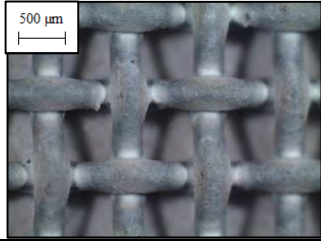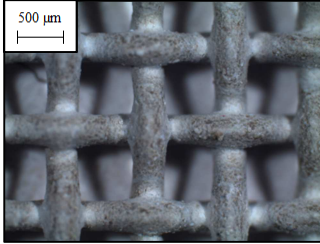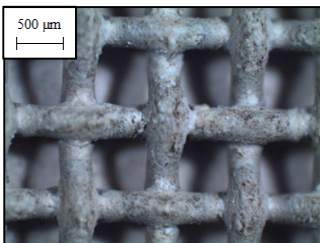
Structured catalyst	Method of Sn Addition	Specific loading (mg/cm²)	Bulk Sn/Ti	Bulk Sn % (SD)
M1	-	4.5	-	-
M2	Impregnation of Sn-oxalate	4.2	0.180	2.90 (0.90)
M3	Sn-oxalate added to washcoating suspension	4.9	0.025	0.20 (0.03)
M4	SnO_2 particles added to washcoating suspension	4.2	0.002	0.03 (0.02)
M5	SnO_2 nanoparticles added to washcoating suspension	4.3	0.013	0.22 (0.10)

Table 2. Elemental mapping, in weight %, obtained by SEM/EDS of the fresh M3 catalyst, used M3 catalyst after all tests (> 400 h) and commercial mesh (CM).

Element	Fresh	After 400 h	Commercial mesh (CM)
Oxygen	70.90 ± 2.10	53.29 ± 6.65	20.66 ± 16.41
Zirconium	9.20 ± 0.40	11.01 ± 0.06	n. d.
Titanium	19.60 ± 1.90	19.28 ± 3.80	21.53 ± 8.53
Tin	0.20 ± 0.03	n. d.	n. d.
Carbon	n. d.	9.05 ± 3.94	38.98 ± 3.62
Iron	n. d.	5.44 ± 2.22	n. d.
Ruthenium	n. d.	n. d.	18.28 ± 6.55

n.d. – not detected

Table 3. TiO$_2$ crystallite sizes of the different coatings and their lattice parameters.
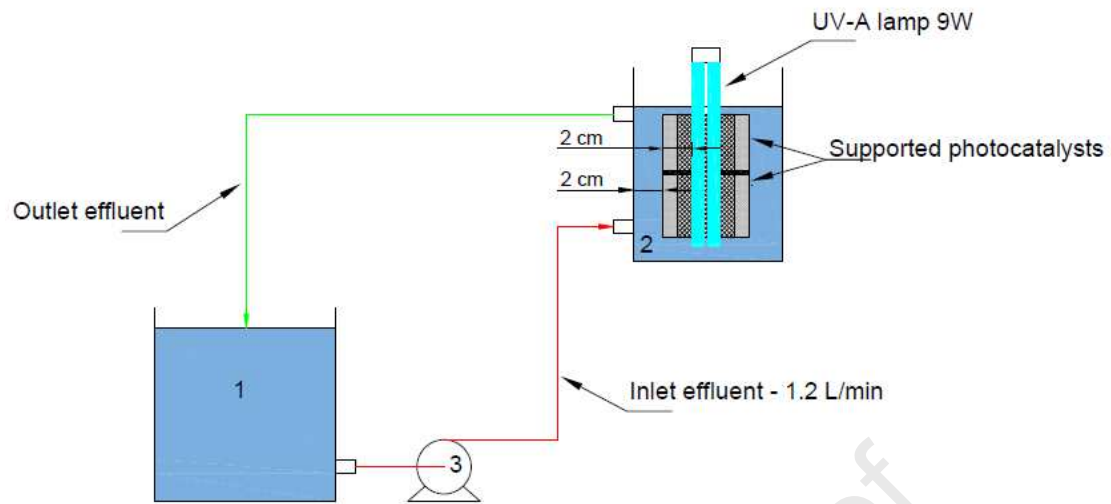
Sample	Lattice constants			Unit cell volume	Interplanar distance	Crystallite size
	a (Å)	b (Å)	c (Å)	(Å^3)	d (Å)	(nm)
M1	3.786	3.786	9.509	136.303	3.531	13.82
M2	3.785	3.785	9.501	136.088	3.537	20.98
M3	3.791	3.791	9.521	136.856	3.542	18.02
M4	3.779	3.779	9.480	135.385	3.650	19.84
M5	3.781	3.781	9.500	135.809	3.541	20.54
TiO$_2$ Anatase [a]	3.785	3.785	9.512	136.262	3.516	-
SnO$_2$ cassiterite [b]	4.738	4.738	3.187	71.55	3.347	-

[a] Data from JCPDS Card nᵒ 01-084-1285

[b] Data drom JCPDS Card nᵒ 00-041-1445

Table 4. Surface data of the Sn-doped structured photocatalysts.

Structured catalyst	Main peak BE of Sn 3d$_{5/2}$ (eV)	Main peak BE of Ti 2p$_{3/2}$ (eV)	Main peak BE of Zr 3d$_{5/2}$ (eV)
M2	486.3 (1.9)[a]	458.5 (1.5)	182.0 (1.8)
M3	486.2 (1.9)	458.4 (1.5)	182.1 (1.8)
M4	486.6 (1.7)	458.6 (1.5)	182.1 (2.2)
M5	486.3 (1.9)	458.4 (1.5)	182.1 (1.9)

[a] FWHM in parenthesis.

UV-A lamp 9W

2 cm

2 cm

Supported photocatalysts

Outlet effluent

Inlet effluent - 1.2 L/min

1

2

3

Fig. 1.

The table embedded in panel (b):

Catalyst	k (min⁻¹)
M1	0.04349
M2	0.04283
M3	0.04653
M4	0.03184
M5	0.02764
CM	0.02565
DP	0.02672

Fig. 2.

(a) Type I   **(b)** Type II   **(c)** Type III
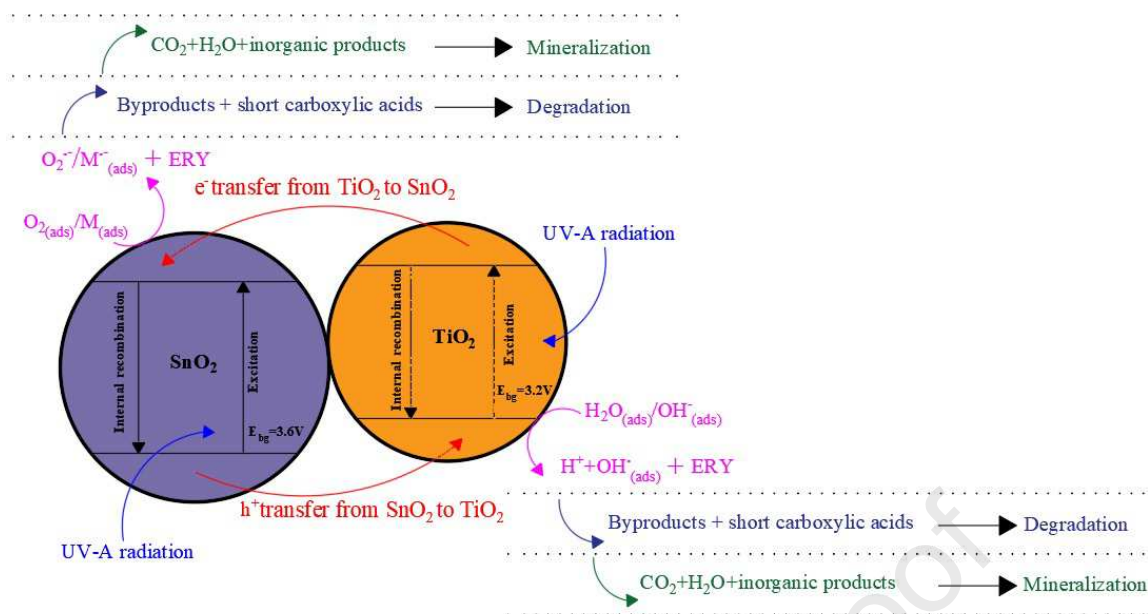
Fig. 3.

Fig. 4.
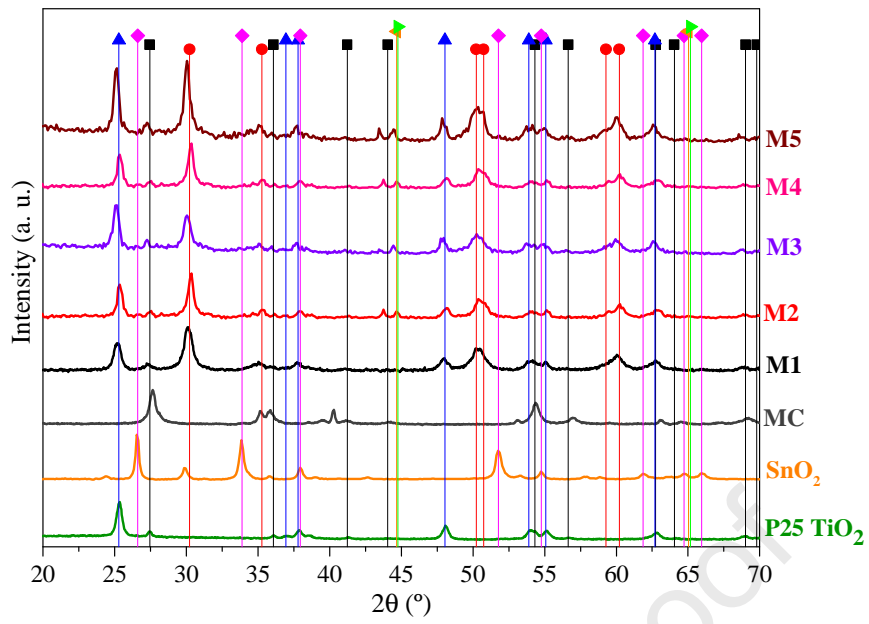
(a)

(b)
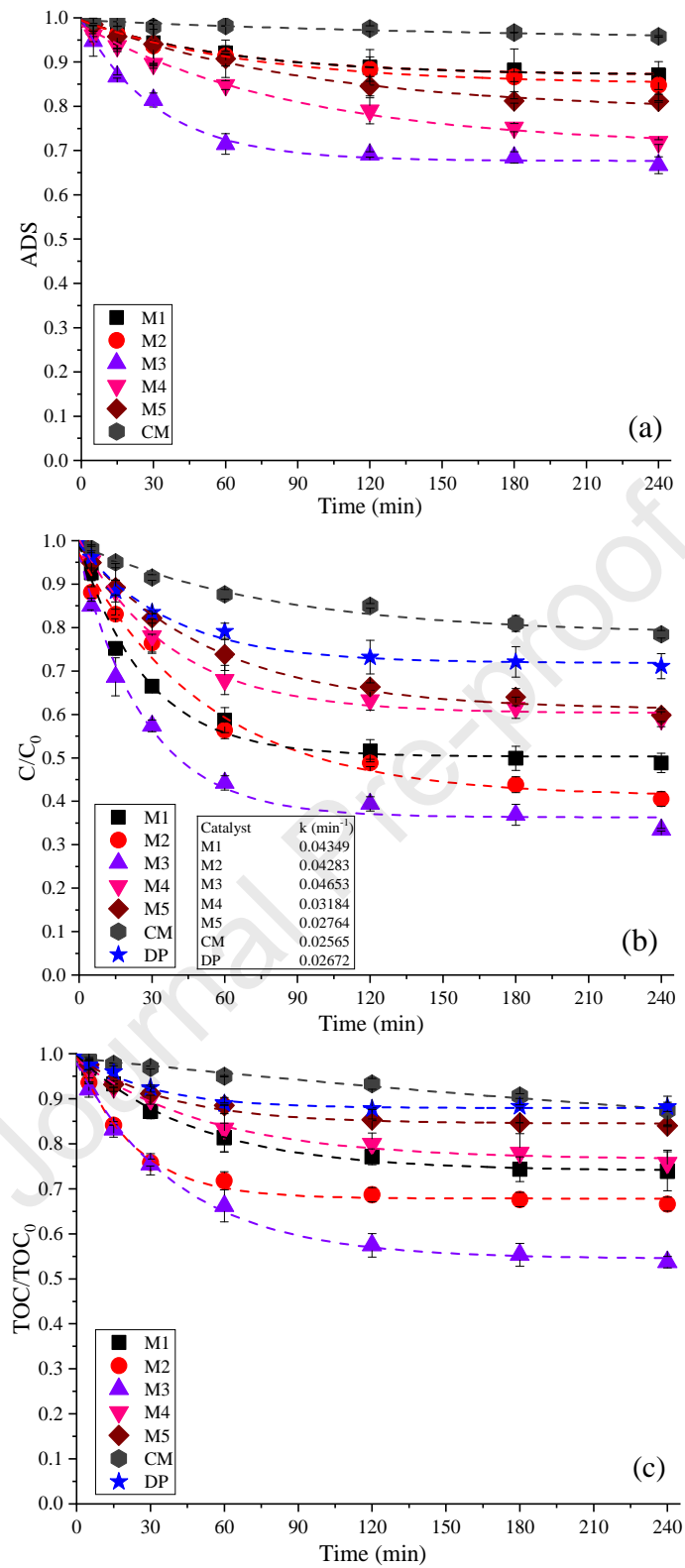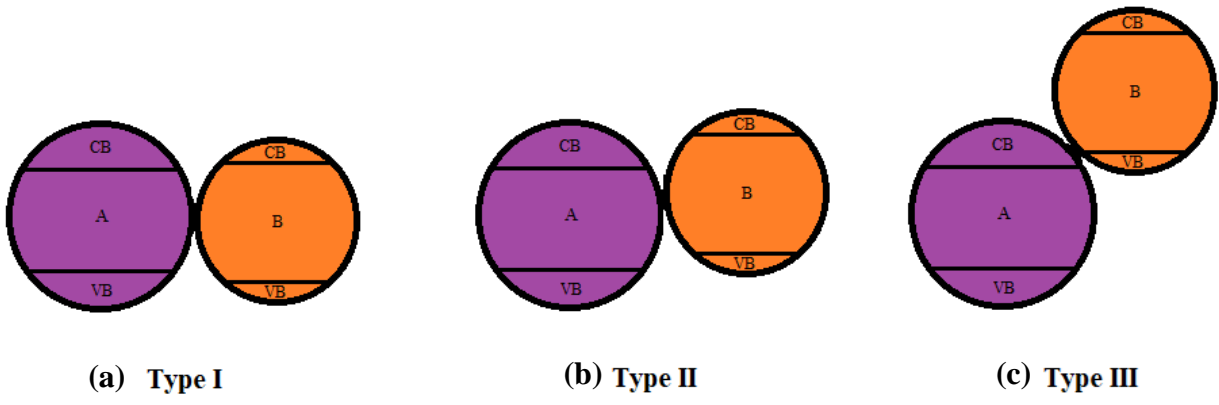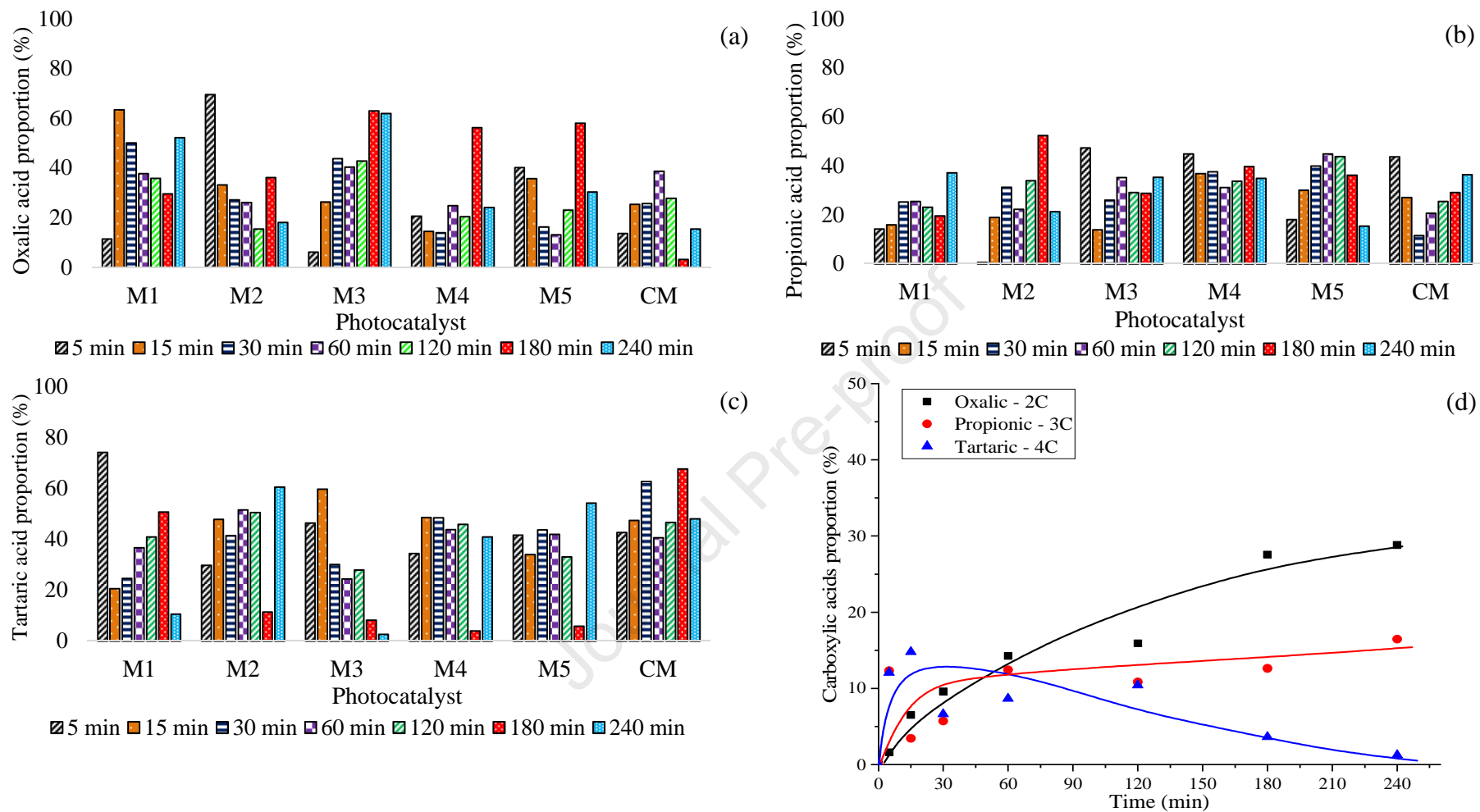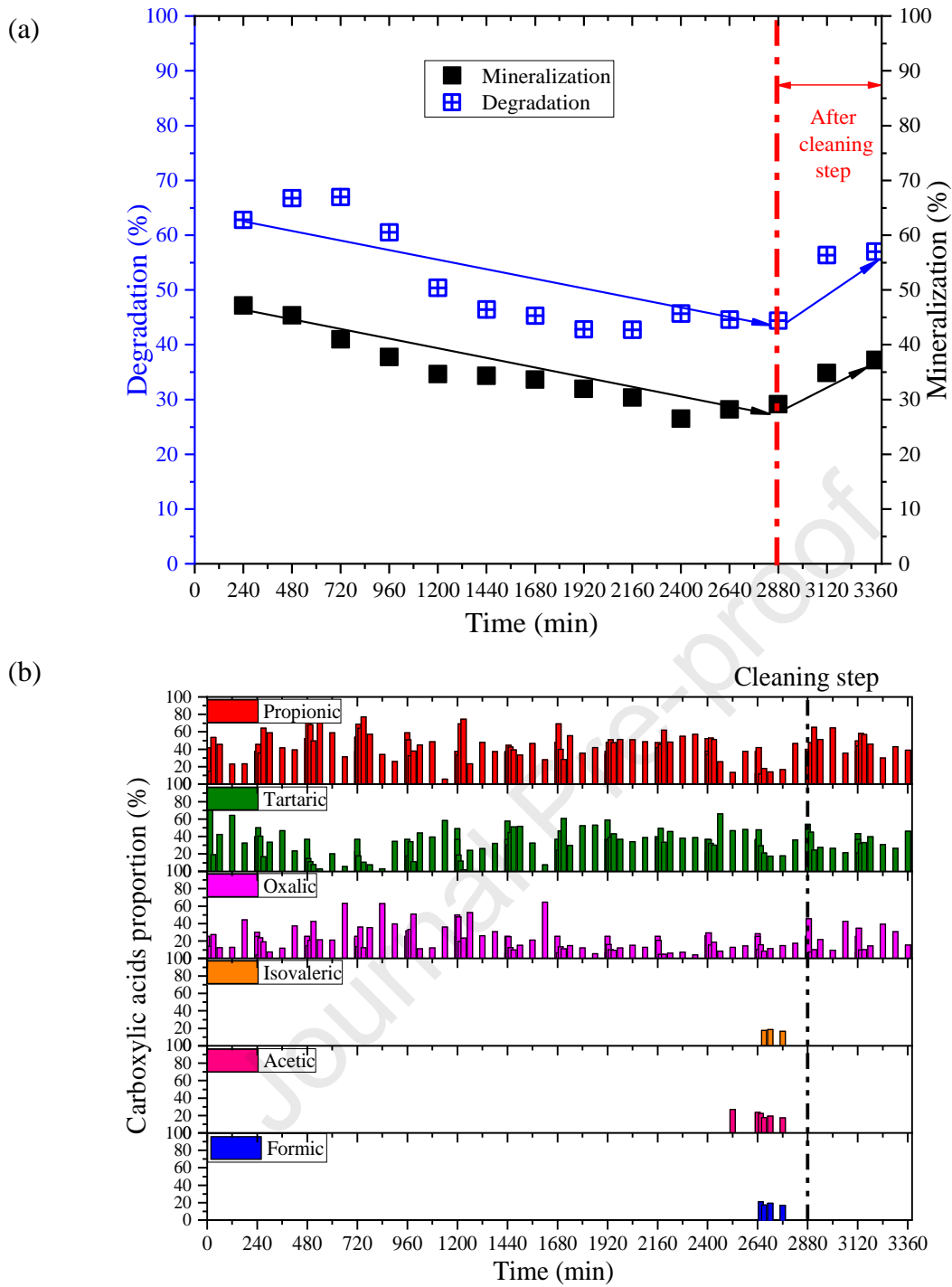
Fig. 5.

Fig. 6.

Fig. 7.

HIGHLIGHTS

- SnO_2-doped TiO_2 increases the mineralization and degradation of ERY in relation to TiO_2.

- Sn addition sources and methods affected the catalyst performance.

- Formation of low molecular weight carboxylic acids were detected.

- ERY oxidation pathway onto $Ti_{1-x}Sn_xO_2$ staggered gap are proposed.

- The prepared catalyst showed high catalytic activity after more than 400 h of use.

Declaration of interests

☒ The authors declare that they have no known competing financial interests or personal relationships that could have appeared to influence the work reported in this paper.

☐The authors declare the following financial interests/personal relationships which may be considered as potential competing interests: